DOE/ER/79048-1

SuperBall: A 4π NEUTRON DETECTOR FOR CALORIMETRIC STUDIES OF INTERMEDIATE-ENERGY HEAVY-ION REACTIONS

Performance and Final Report
September 30, 1991 - March 30, 1995

W.U. Schröder

University of Rochester
Rochester, New York 14627

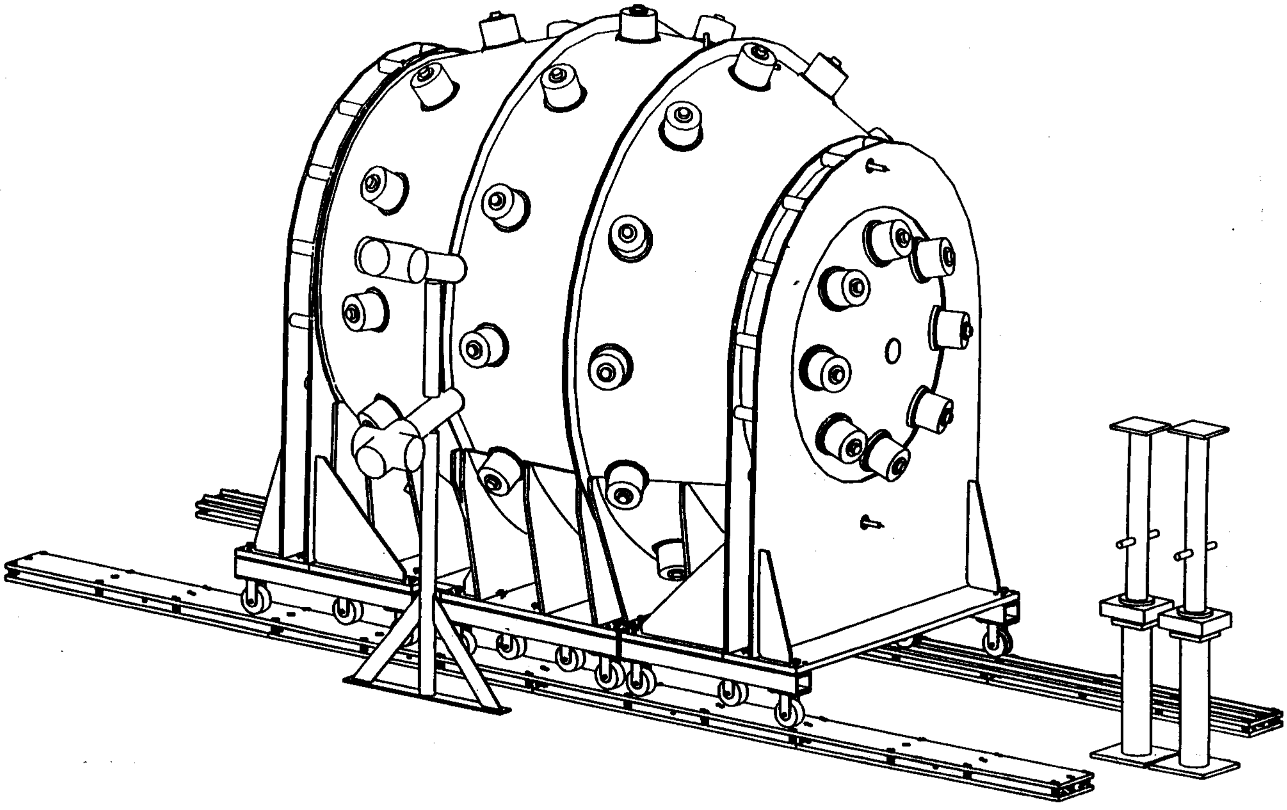

March 1995

Prepared for The U.S. Department of Energy
Agreement No. DE-FG05-91ER79048

DOE/ER/79048-1

SuperBall: A 4π NEUTRON DETECTOR FOR CALORIMETRIC STUDIES OF INTERMEDIATE-ENERGY HEAVY-ION REACTIONS

Performance and Final Report
September 30, 1991 - March 30, 1995

W.U. Schröder

University of Rochester
Rochester, New York 14627

March 1995

Prepared for The U.S. Department of Energy
Agreement No. DE-FG05-91ER79048

NOTICE

This report was prepared as an account of work sponsored by the United States government. Neither the United States nor the United States Department of Energy, nor any of their employees, nor any of their contractors, subcontractors, or their employees, makes any warranty, express or implied, or assumes any legal liability or responsibility for the accuracy, completeness, or usefulness of any information, apparatus, product, or process disclosed or represents that its use would not infringe privately owned rights.

Abstract

A 16,000-liter, 5-segment 4π neutron calorimeter, The Rochester *SuperBall*, has been designed, constructed, and tested in off-line and in-beam measurements. The device is a scintillation detector using Gd-loaded organic liquid as a scintillator. The *SuperBall* allows one to measure, event by event, with high efficiency, and as a function of angle, the numbers and the total kinetic energy of neutrons emitted in a nuclear reaction. These observables provide information on the energy dissipated in a nuclear collision and the collision impact parameter. Equipped with a large internal vacuum chamber, the *SuperBall* can be operated in conjunction with 4π charged-particle detector arrays, providing full coverage of all light particles emitted in a reaction. In September-December of 1993, the *SuperBall* was installed at the MSU National Superconducting Cyclotron Laboratory, where it is being used for studies of the mechanisms of intermediate-energy heavy-ion reactions. The first in-beam test experiment with the *SuperBall* was conducted in December 1993. In its first production experiment, the study of new process of super-slow heavy residue (HR) production in coincidence with projectile-like fragments in the reaction ^{197}Au+^{86}Kr at E/A = 35 MeV, the *SuperBall* was used in combination with a *4π* charged-particle detector and a series of silicon strip detectors and telescopes. In the most recent experiment (March 1995) on the reaction ^{112}Sn +^{112}Sn at E/A=40 MeV, the *SuperBall* was used in conjunction with the *MiniBall/Wall 4π* charged-particle arrays and various other Si/CsI detector arrays. The results of these measurements demonstrate an excellent performance of the *SuperBall*, reaching all design goals, and illustrate the significant new information on the reaction mechanism gained with this detector. Detector performance is discussed in the context of the results achieved in the recent experiments.

Table Of Contents

Abstract 2

Table of Contents 3

I. Introduction 4

II. The Neutron Multiplicity Observable 7

III. Design Requirements And Characteristics Of Neutron Calorimeters 20

IV. Mechanical Design 36

V. Liquid-Scintillator And Reflectance Tests 49

VI. Electronics 56

VII. *SuperBall* Construction And Installation 64

VIII. Detector Performance Tests 77

IX. Summary And Outlook 96

X. Acknowledgments 97

XI. References 99

I. Introduction

The study of nuclear reactions at bombarding energies sufficiently high to disassemble the interacting system to a large extent requires a multitude of different and highly efficient detection systems. The *SuperBall* neutron calorimeter described in this report is one such device, intended initially for applications in heavy-ion reactions at bombarding energies of a few tens of MeV per nucleon, i.e., in the Fermi energy regime, and, later on, also in the intermediate-energy regime of a few hundred MeV per nucleon. The currently significant experimental and theoretical interest in intermediate-energy heavy-ion reactions is generated largely by the expectation of qualitatively new reaction phenomena [Ber88, Bon85, Bar90, Gro86,87,93, Fri88,90, Lop89,90] at nucleus-nucleus approach velocities comparable with the nucleonic Fermi velocities. In this transitional bombarding energy regime, the dominance of the mean field should give way to a growing importance of two-body nucleon-nucleon collisions [Gre86, Ayi87, Ber88] and higher nucleonic correlations, resulting in significant fluctuations in experimental observables. In addition, non-adiabatic effects in the effective conservative and dissipative nuclear interactions may be encountered [Sch84, Nör86] that should manifest themselves in a characteristic bombarding-energy dependence of collective scattering phenomena. More dramatic reaction phenomena such as nuclear vaporization or instantaneous multi-fragmentation could occur, provided that critically high excitation energies per nucleon of $\varepsilon^* \sim 5\text{-}6$ MeV [Lev87, Sur87,89] are reached in the interacting nuclear systems. The occurrence of nuclear multi-fragmentation has been associated with a nuclear liquid-gas phase transition. Alternatively, and not less interestingly, nuclear multi-fragmentation has been related [Mor92] also to a macroscopic, Rayleigh-type instability of hot nuclear matter, discussed previously [Bro89] in the context of nuclear fission and low-energy heavy-ion reactions.

Experimentally, however, no direct demonstration of instantaneous multi-fragmentation or vaporization, concurrent with the macroscopic collision, is available yet, nor have other expected transitional features such as unusually large fluctuations in experimental fragment distributions been demonstrated unambiguously. Nevertheless, the observation of a copious production of intermediate-mass fragments (IMF), followed by a disappearance of this decay mode at higher bombarding energies, has already been taken [Mor88, Kim92, Ogi92], if tentatively, as indication of such new reaction modes.

In this experimentally unsettled situation, a systematic tracing of the reaction phenomenology, from bombarding energies of a few MeV per nucleon into the Fermi energy regime, appears to be a most promising strategy to study the transitional features of the reaction mechanism. Such systematic studies have just been initiated. Some of the difficulties and ambiguities with existing experimental data are undoubtedly related to the nature of reaction systems measured thus far. With only relatively few exceptions, these past studies have considered reactions induced by ^{40}Ar or lighter projectiles. These reactions exhibit a rich phenomenology already at relatively low bombarding energies, including the processes of quasi-elastic, damped, incomplete fusion/massive transfer, complete fusion-evaporation and fusion-fission reactions. At the higher energies of interest here, additional processes of fragmentation [Gol74, Fri83] or participant-spectator reactions [Day86, Bon87, Gra88] are expected to further complicate the picture. Yet another complication is due to the fact that the mass range from light charged particles and IMF's to projectile-like fragments is often very narrow, making a distinction between the various product types difficult.

Reactions between very heavy nuclei, on the other hand, are associated with a very broad range of reaction products, where even relatively small remnants of PLF's, having undergone a partial disassembly, are clearly separated in mass from IMF's and light charged particles. If governed by dissipative dynamics similar to that well known from lower bombarding energies [Sch84], these reactions are expected evolve smoothly with bombarding energy and impact parameter. In front of such a smooth background, the onset of a new type of mechanism should be highly visible. Although even reactive changes akin to a "phase" transition would not occur suddenly at the approach of a critical point, because of the finite size of nuclei, the effect would be largest for the heaviest systems. From studies at lower bombarding energies, one knows [Sch84] that there is a fairly well defined correlation between impact parameter and the amount of energy dissipated in a reaction, the "energy loss" E_{loss}, or equivalently, with the amount of heat energy generated in the massive reaction products. Initial studies suggest [Bar92] that similar correlations exist also in the Fermi energy regime, in which case the impact parameter range contributing to a certain process can be deduced from the multiplicities of the particles evaporated from the corresponding fragments.

Drastic, if not catastrophic, changes in the behavior of a nuclear system have been predicted to occur [Ber88, Bon85, Gro86,87,93, Fri88,90, Lop89, 90], either if the nuclear temperature is raised to sufficiently high levels, or if an initially highly compressed nucleus in its expansion phase passes through the spinodal (negative-compressibility) region. In either case, the nucleus should be highly excited, with the balance between thermal and collective excitation determined largely by the frequency of in-medium nucleon-nucleon collisions and the equation of state. One of the most important experimental tasks is then to create nuclear systems with demonstrated high excitation energies per nucleon, ε^*, or temperatures τ, used here as an approximate concept. Critical temperatures are expected [Lev87] to be of the order of $\tau_{crit} \approx 6$ MeV, for stable heavy nuclei ($A \approx 220$). No predictions are available for systems as heavy as $A = 400$-480, which one may be able to produce in a collision between very heavy ions. Another, equally important task consists in a characterization of the decay of such systems as unambiguously as possible, which implies a measurement of as many secondary particles as possible.

The question then arises as to how to produce heavy, relatively unstable, e.g., neutron-poor, systems with specific thermal excitations of $\varepsilon^* \geq 6$-7 MeV and how to measure such high excitation energies. The experimental task can be accomplished either by a complete measurement of the kinematics of a multi-particle event or by an exclusive study of the evaporative and fission-like decay of the hot primary reaction products. In view of the large particle multiplicities, the second technique appears to be more feasible. For the very heavy systems of interest here, this latter technique invariably requires an efficient measurement of the neutrons emitted in a reaction event. This has been the motivation for the development of a large, highly efficient, neutron calorimeter, the Rochester *Super-Ball*, which will be described in Sections III and IV. First, however, recent evidence for the importance of the multiplicity of neutrons as an observable indicating high excitations will be reviewed briefly in the following Section II.

II. The Neutron Multiplicity Observable

As discussed in the previous section, it is an important experimental task to deduce the intrinsic, "thermal" excitation energy deposited in the primary products of an energetic nuclear collision. For bombarding energies at the lower boundary of the Fermi energy regime, pre-equilibrium emission of nucleons in a collision is not a very important process. For higher bombarding energies, this process can limit very effectively the energy deposition into the fragments [Sch92] and complicate the inference of product excitation energies, or associated impact parameters, from the emitted light particles. Since one is mainly interested in very heavy systems, all primary reaction products are expected to be neutron-rich, but to decay sequentially, foremost by the statistical evaporation of neutrons. Neutron emission is unhindered by emission barriers and, hence, evaporation times can be a short as $t_{evap} \sim 10^{-22}$ s. On a longer time scale, emission of light charged particles (lcp) and IMF's follows, as predicted by statistical-model calculation, including models considering an expanding emitting source [Fri83].

So far, there have been very few measurements yielding information on the neutron/light-charged-particle branching ratio. A systematic study has been performed for the asymmetric system ^{232}Th+^{40}Ar [Jia89] for ^{40}Ar energies up to E/A = 77 MeV. This study shows that, with the bombarding energy increased from E/A = 10 MeV to E/A = 50 MeV, there is a strong increase in the average multiplicity of emitted neutrons, i.e., in the thermal energy deposit in the system. At higher bombarding energies, the particle multiplicities increase only relatively slowly, which has been interpreted as a saturation occurring in the thermal energy deposition. At the higher energies, the ratio of the multiplicities of neutrons to charged particles with Z = 1,2, emitted in the ^{232}Th+^{40}Ar reaction, has been estimated [Jia89] to be approximately equal to $m_n/m_{lcp} \approx 6$. One also estimates [Jia89] that most of the energy dissipated in a collision, approximately 550 MeV of the total 700 MeV, is carried away by neutrons. Although such a dependence is qualitatively expected from the smaller transmission coefficients for charged particles, the magnitude of the effect is perhaps at first surprising.

Particle branching ratios have been measured [Sch92] rather effectively in a recent ^{209}Bi+^{136}Xe experiment at E/A = 28 MeV, since it entailed a simultaneous 4π measurement of charged particles and neutrons. Hence, one can study multiplicity correlations of the kind exhibited in Fig. II.1. In this figure, the joint multiplicity distribution is plotted in a two-dimensional contour diagram *vs.* the multiplicity of neutrons and the multiplicity of light charged particles, neither one corrected for the finite detection efficiency or solid angle. In the ^{209}Bi+^{136}Xe experiment, this correction was larger for the neutrons, since the efficiency of the relatively small neutron detector was only $\varepsilon \approx 0.5$-0.6, while the coverage for the charged particles was better than 75% of 4π. However, the important features of the multiplicity correlation of Fig. II.1 are clear: The neutron multiplicity observable covers, with good accuracy, the entire range of dissipated energies and, hence, also of the associated impact parameters. Approximately 30-35 neutrons are emitted with very little competition by charged particles. This is indicated by the vertical portion of the yield ridge in Fig. II.1, for low and intermediate neutron multiplicities. Only for more dissipative collisions, i.e., events associated with higher neutron multiplicities, does charged-particle emission become noticeable. For these higher energy losses, the two multiplicities correlate rather well with one another, and here either observable can be used to characterize the degree of dissipation.

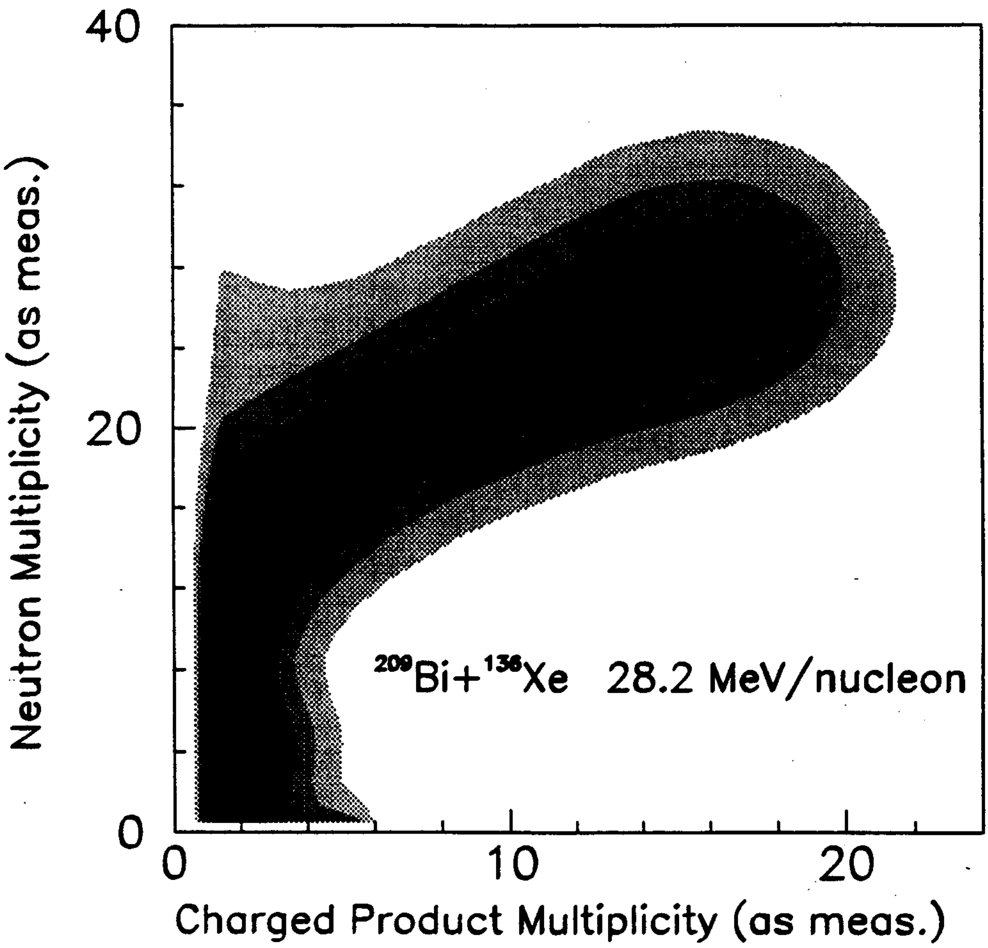

Fig. II.1: Contour diagram of the joint multiplicity distribution for the ^{209}Bi+^{136}Xe reaction at 28 MeV/u, plotted *vs*. multiplicities of neutrons and of light charged particles, as measured. The efficiency is $\varepsilon \approx 0.5$-0.6 for the neutrons and $\varepsilon \approx 0.75$ for charged particles.

Statistical-model calculations, assuming the particles to be evaporated sequentially from the hot primary Bi- or Xe-like fragments can quantitatively reproduce the average multiplicity correlation, i.e., the ridge line in Fig. II.1, with the important result that the intrinsic excitation of these reaction fragments can be deduced from the experimental particle multiplicities. Some detailed results of the calculations are shown in Fig. II.2, for two different isotopes of Xe representing the primary projectile-like fragment, and a range of excitation energies. One observes that heavier charged particles are emitted only in more dissipative collisions associated with a significant neutron multiplicity. This effect is strongly dependent on the neutron richness of the emitter fragment, as one infers from a comparison of the calculations for ^{129}Xe and ^{136}Xe depicted on the top and bottom, respectively, of Fig. II.2.

From the comparison of these theoretical calculations to experimental data, one gathers that the neutron multiplicity in particular represents a sensitive measure of the excitation energy of the emitter and, therefore, of the amount of energy dissipated in a reaction. On average, the amount of excitation energy carried away by a particle of average binding energy $\langle B \rangle$ is given by

$$\delta\ E^* = \langle B \rangle + V_C + 1.5 \cdot \tau \qquad \text{(II.1)}$$

where V_C is the emission barrier and τ denotes the temperature of the daughter nucleus. The smaller the sum of binding energy and barrier of a given type of light particle, the better the resolution of the excitation energy measurement by the corresponding particle multiplicity. Since $V_C = 0$ for neutrons, the neutron multiplicity provides the most accurate measure of the excitation energy.

In addition, since the neutron binding energies per nucleon do not vary appreciatively with the mass number of the nucleus, the number of neutrons emitted, for a given total nuclear excitation energy, does not depend significantly on the nuclear species and the number of emitting reaction products. This appears to be true even for relatively light

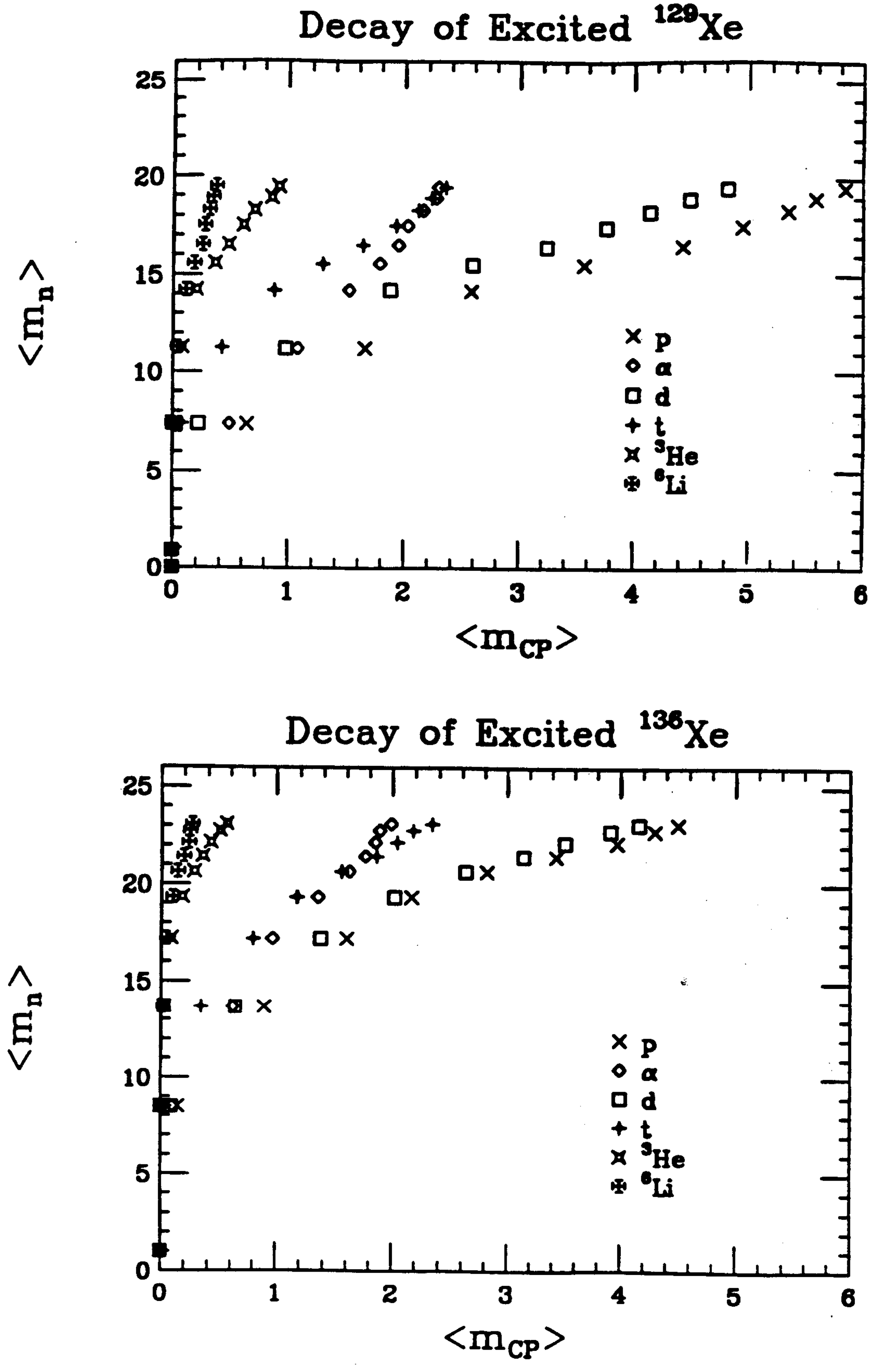

Fig. II.2: Theoretical correlations between the multiplicity of neutrons and the multiplicity of various charged-particle types evaporated from excited fragments ^{129}Xe (top panel) and ^{136}Xe (bottom panel) are illustrated by the symbols explained in the legend. The calculations were done with the code EVAP [Nic92].

primary products from reactions induced with very heavy systems. Although the barrier hindering charged-particle emission from such lighter products is relatively small, these fragments are also very neutron-rich, which counter-balances the effect of increased charged-particle transmission coefficients. The predominance of neutron emission is, of course, very important for a calorimetry of neutrons in nuclear reactions, that is based on a measurement of the multiplicity of neutrons. It allows at least an approximate determination of the total amount of kinetic energy loss, or more precisely, of the amount of intrinsic heat energy generated in a collision, a quantity that was found [Sch84] to be indicative of the collision impact parameter. A similar effect does not exist for charged particles, where the atomic number Z of the emitting fragments play a more important role.

However, the multiplicity of neutrons, or of any other evaporated particle, is generally not a linear function of the excitation energy E^* of the emitting nucleus. This is due to the fact that the cumulative binding energy $B(\mathrm{m})$ for m particles increases approximately quadratically with m. The resulting non-linearity is demonstrated in Fig. II.3 for neutrons emitted from excited ^{197}Au nuclei. In this figure, the probability is plotted *vs* the neutron multiplicity, for different excitation energy distributions of the ^{197}Au nuclei. A simplified neutron evaporation calculation [Sch80] has been performed, neglecting the competition by other light particles in the evaporation process, which is well justified for the present purpose. An excitation energy distribution, which is constant up to a maximum energy noted at the various histograms in Fig. II.3, has been assumed for the ensemble of ^{197}Au nuclei. As can be seen from Fig. II.3, one obtains multiplicity distributions that increase linearly with increasing with multiplicity. The cut-off of the distributions at high multiplicities is determined by the widths of the neutron kinetic-energy distributions, i.e., the "temperature" or logarithmic slope parameter of the neutron spectra in the rest frames of the respective emitters. Such a behavior is expected, since the multiplicity bin with is determined by $\mathrm{d}B/\mathrm{dm}$. For the same reason, the upper edge of the multiplicity distribution, as well as the most probable neutron multiplicity do not move to higher multiplicity values, as the maximum excitation energy of the emitting nucleus is increased. This non-linearity is increased, if proper account is taken of the effect of charged-particle competition in the

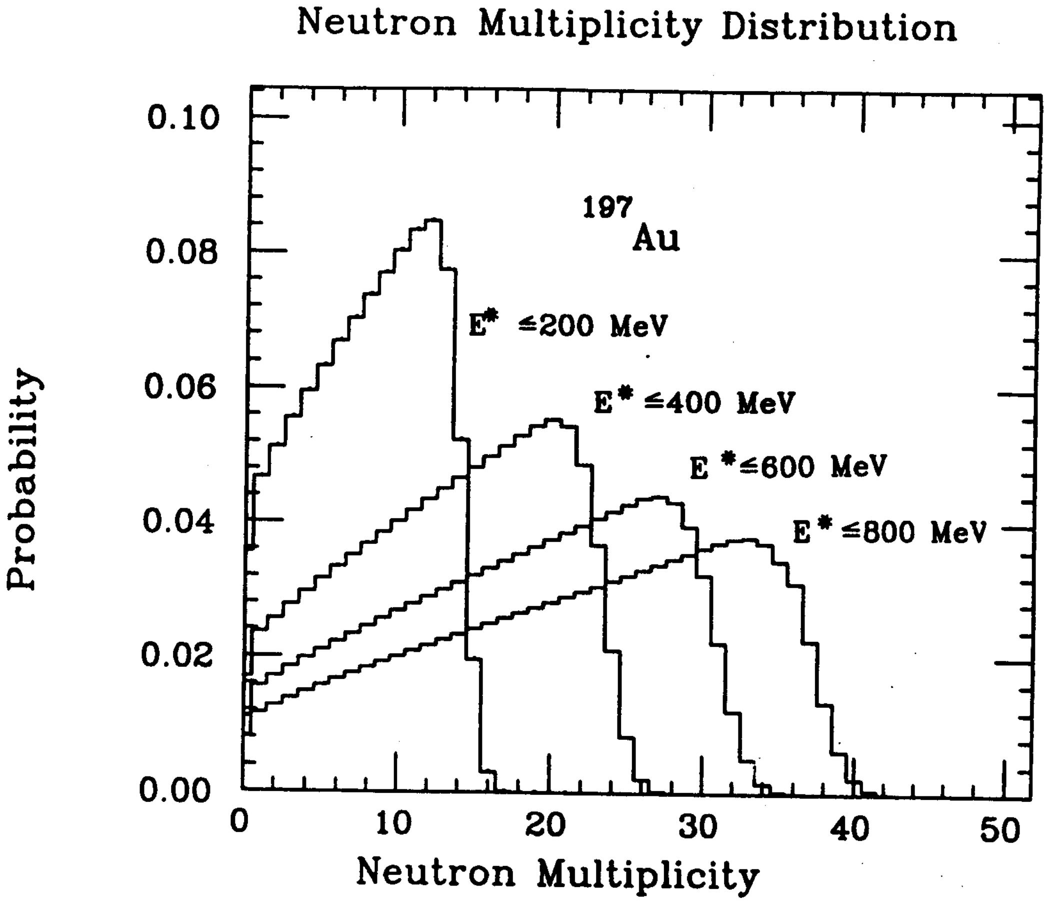

Fig. II.3: The theoretical probability is plotted for the multiplicity of neutrons emitted from ^{197}Au nuclei, for uniform excitation energy distributions of the ^{197}Au nuclei with maximum excitation indicated at each histogram. These are results of a simplified neutron evaporation calculation [Sch80a].

evaporation cascade. Similar considerations apply to multiplicity distributions of charged particles.

As emphasized above, the neutron multiplicity is expected to provide the most accurate measure of the excitation energy, as long as the binding energies of the competing particles are comparable to or larger than the neutron binding energy. However, the non-linear effects discussed above become increasingly important for long neutron evaporation chains, where the average neutron binding energy can become rather large, such that charged-particle emission competes effectively with neutron evaporation. To illustrate the effect, Fig. II.4 shows experimental data [Que93] for the correlation between average neutron multiplicity, m_{tot}, and the total kinetic energy loss, E_{loss}, for the reaction $^{197}Au+^{208}Pb$ at E/A = 29 MeV. The various symbols indicate different trigger conditions selecting event with different energy losses, which are determined independently from kinematics. The curve drawn through the data represents a realistic evaporation calculation [Que93] using the code EVAP [Nic92]. As can be inferred from the slope of the data in Fig. II.4, although the correlation $m_{tot}(E_{loss})$ is rather well defined, the curve becomes somewhat less steep for energy losses larger than 1 GeV.

Since the evaporation calculations represent the multiplicity data of Figs. II.1 and II.4 rather well, statistical-model predictions for the accuracy in determining the excitation energy E^* of a heavy nucleus should be realistic also. Therefore, in Fig. II.5, the quantities $(\Delta E^*/E^*)_i=(dE^*/dm_i)\Delta m_i/E^*$, related to the energy resolutions obtainable through a measurement of the average multiplicity $m_i(E^*)$of particle type *i*, are plotted vs the excitation energy E^*, of a ^{208}Pb nucleus. Here, $\Delta m_i(E^*)$ is the width of the multiplicity distribution. From Fig. II.5, one observes that, while the best energy resolution ($\Delta E^* \approx 8\%$) is afforded by the joint measurement of the multiplicities of all particles, the neutron multiplicity represents a more accurate measure than that of protons or alpha particles, for interesting nuclear excitation energies. This is particularly true for small to medium excitation energies, and correspondingly, for partially damped heavy-ion reactions of medium to large impact parameters. These data are for an ideal detector measuring the entire

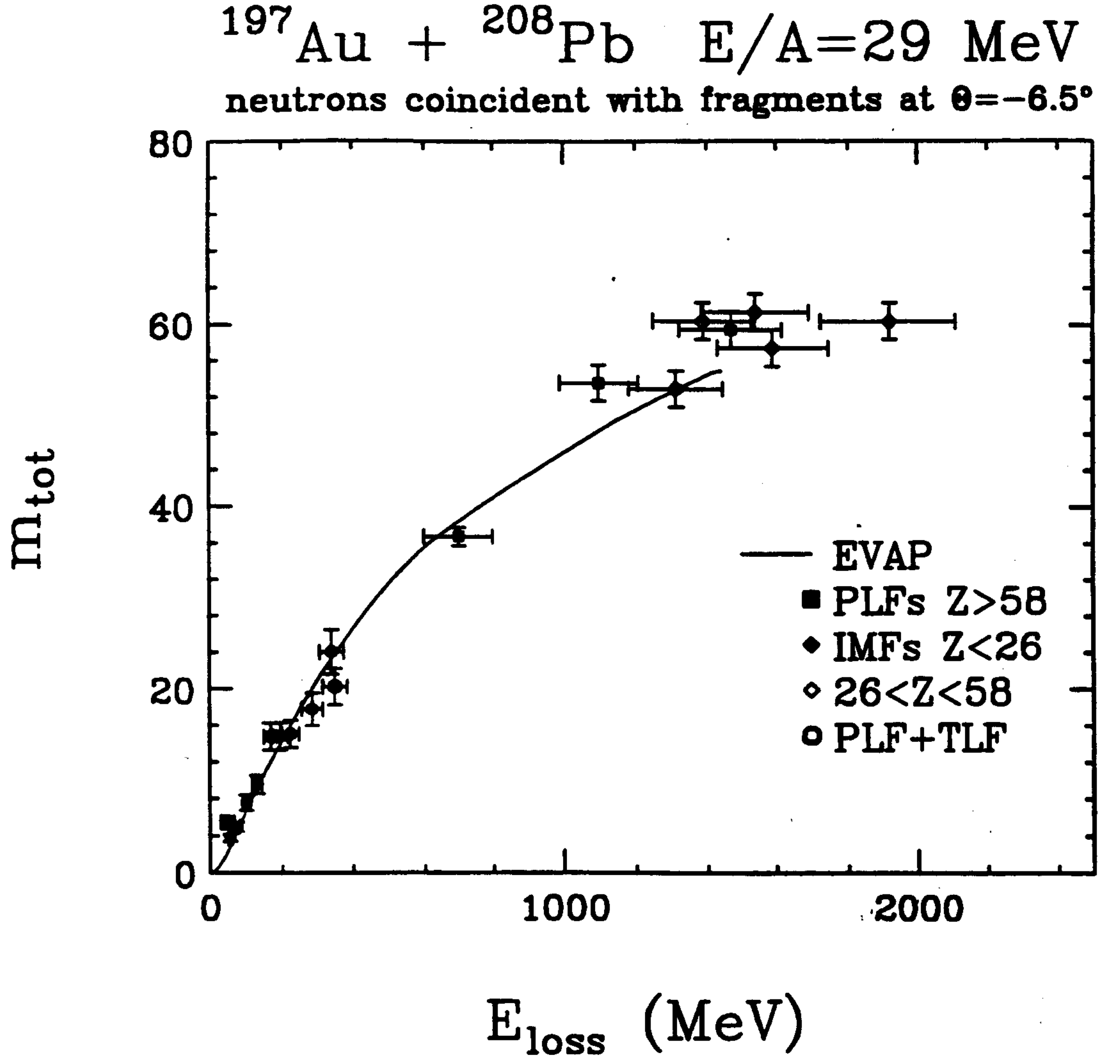

Fig. II.4: The measured total neutron multiplicity m_{tot} is plotted *vs*. a kinematically determined total kinetic-energy loss E_{loss} in the reaction ^{197}Au+^{208}Pb at 29 MeV/u [Que93b]. The various symbols indicate different trigger conditions, while the full curve represents an evaporation calculation, assuming sequential evaporation from Au and Pb fragments.

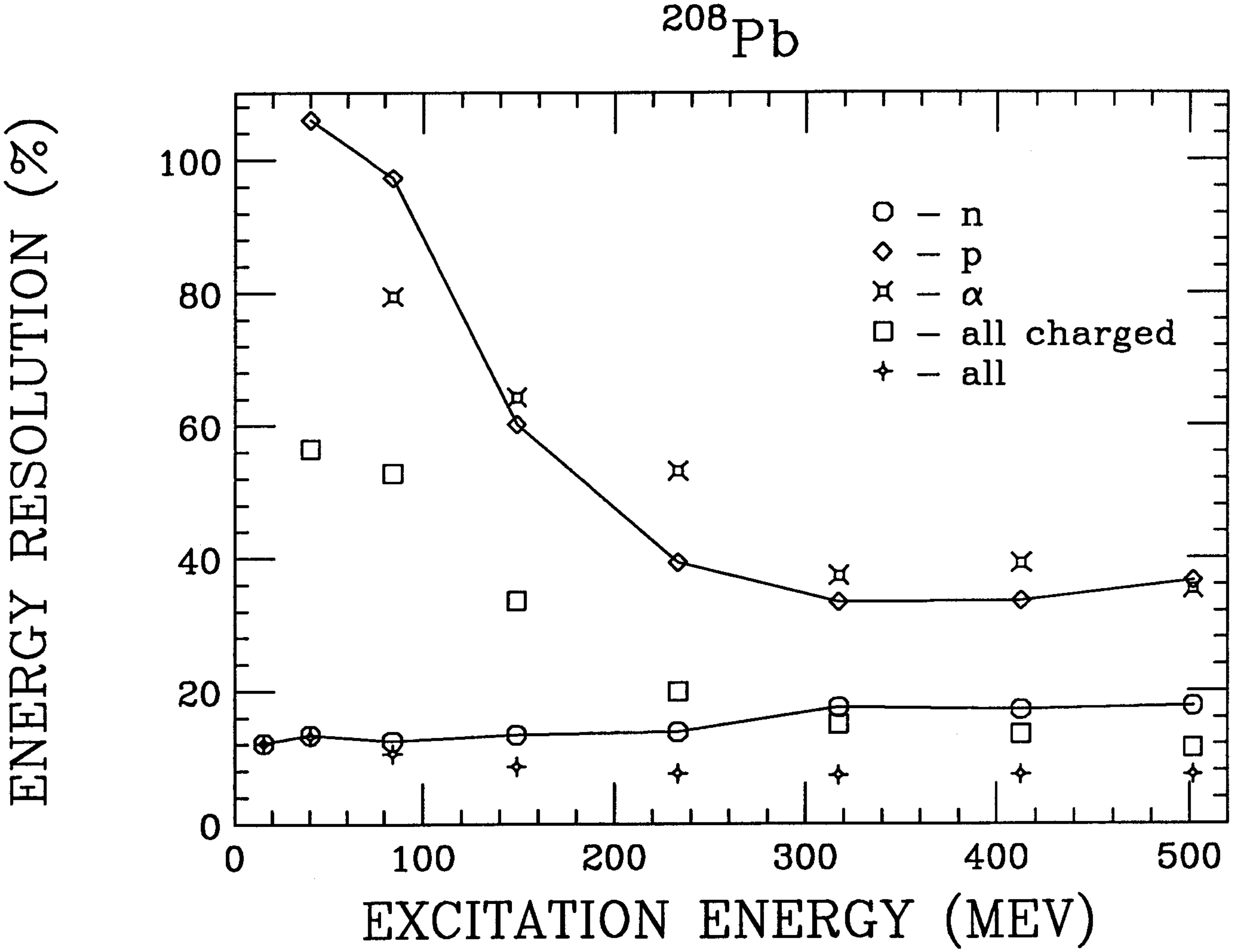

Fig. II.5: The quantities $(\Delta E^*/E^*)_i=(dE^*/dm_i)\Delta m_i/E^*$, related to the energy resolutions obtainable through a measurement of the average multiplicity $m_i(E^*)$of particle type *i*, are plotted vs the excitation energy E^*, of a ^{208}Pb nucleus.

spectrum for each particle type with unit efficiency. Most real detectors miss a significant fraction of the low-energy portions of the charged-particle spectra and have a significantly less than unit efficiency for neutrons, such that the actual resolution figures are much worse than those illustrated in Fig. II.5. Nevertheless, this figure demonstrates that 4π, high-efficiency neutron counting is a very powerful method to deduce the excitation energy of massive products of heavy-ion reactions , for a large range of energy losses and, hence, of impact parameters.

It is worth mentioning already here that *SuperBall* neutron detector has a high detection efficiency, due, to a large extent, to the fact that no lower threshold is imposed on the neutron energy spectrum. It will, therefore, provide reasonably accurate information on the shape of the neutron multiplicity and excitation energy distributions, not only on the averages. Returning to Fig. II.1, one notices that there is a peak in the joint multiplicity distribution, at low multiplicities, and a local maximum at large multiplicities, corresponding to efficiency-corrected multiplicities of $(m_n, m_{lcp}) \approx (52, 20)$. The peak at small multiplicities is due to peripheral, quasi-elastic reactions, while the bump at higher multiplicities is ascribed to highly dissipative, more central collisions. As discussed further above, a peak in the multiplicity distribution at large multiplicities is, at least partially, due to the non-linear dependence of the cumulative binding energy on the multiplicity of neutrons emitted.

Similar features have been seen also for other systems, in the one-dimensional multiplicity distributions, and their equivalents appear in the kinetic-energy loss spectra of damped reactions at lower bombarding energies [Sch84]. For the ^{209}Bi+^{136}Xe reaction, estimates of the excitation energies carried away yield approximately 870 MeV for neutrons and 450 MeV for charged particles, for events in the "central-collision bump". The combined energy of 1.32 GeV carried away by neutrons and charged particles falls somewhat short of the total kinetic energy of 1.96 GeV available above the entrance-channel Coulomb barrier. It seems possible that events in the tails of the distribution sample somewhat higher energy losses, but this needs to be ascertained by further study.

As indicated previously, the multiplicity distributions of neutrons and of lcp's have a characteristic shape featuring a narrow peak at low multiplicities, associated with peripheral collisions, and a broader "central-collision" bump. It is interesting to compare these features of the multiplicity distribution resulting from a heavy-ion reaction with those corresponding to one for a light-ion-induced reaction at the same available excitation energy. Such an example is illustrated in Fig. II.6, comparing the measured, raw multiplicity distributions of neutrons from the reaction of 2-GeV protons (top) and 44-MeV/u ^{40}Ar (bottom) with a ^{197}Au target [Pie93]. The two reactions are different in the size of the hot nuclear system produced in a collision, and in that the approach velocity of the proton is much higher than that of the heavy projectile. The available total excitation energies are E^*_{tot} = 1.98 GeV and 1.46 GeV, and the neutron detection efficiencies of the setup are 0.6 and 0.8 respectively. Both distributions show the same typical shape [Lot93] featuring the "central-collision bump" at high multiplicities. Accounting for an estimated $m_{ne} \approx 4$ non-equilibrium neutrons emitted in the reaction ^{197}Au+p reducing the effective excitation energy for this system, the remaining most probable multiplicity m_{mp} of evaporated neutrons is approximately equal to $m_{thermal} \approx 25$, in good agreement with the most probable multiplicity measured for the ^{197}Au+^{40}Ar reaction. Both systems are heated to similar effective "temperatures", as measured by the multiplicity of evaporated neutrons. The very similar widths of the multiplicity bumps in the p- and ^{40}Ar-induced reactions suggests that the shape of the multiplicity distribution is probably not simply due to a geometrical-overlap effect which would be rather different in the two cases. However, these data demonstrate once again that the neutron multiplicity is a good measure of the excitation energy of hot nuclei produced in a variety of rather different reaction types.

In summary, the above discussion have exemplified the uniqueness and the sensitivity of the neutron multiplicity as a measure of the intrinsic excitation energy of a reaction product, although it should also be kept in mind that the goodness of this measure is somewhat dependent on the constituency of the fragment, in particular its N/Z ratio. At least for products of reactions induced by heavy ions on heavy targets, the neutron mul-

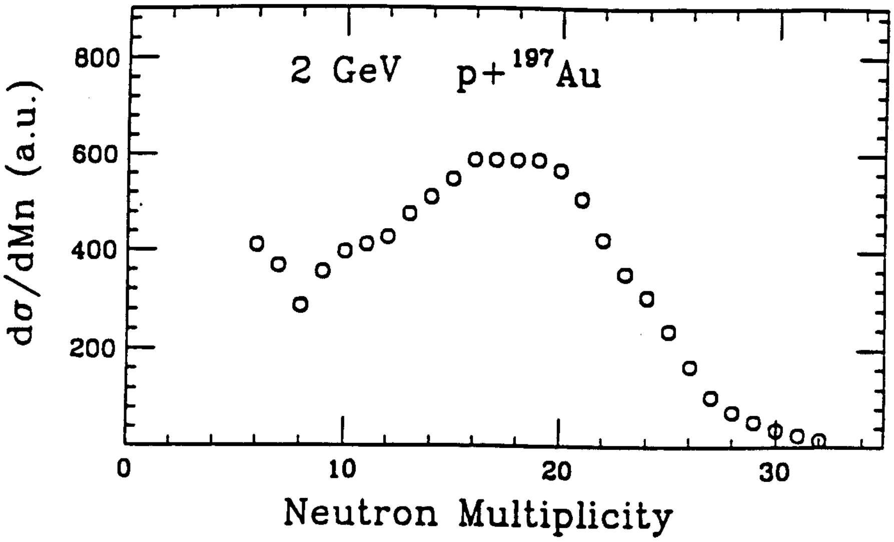

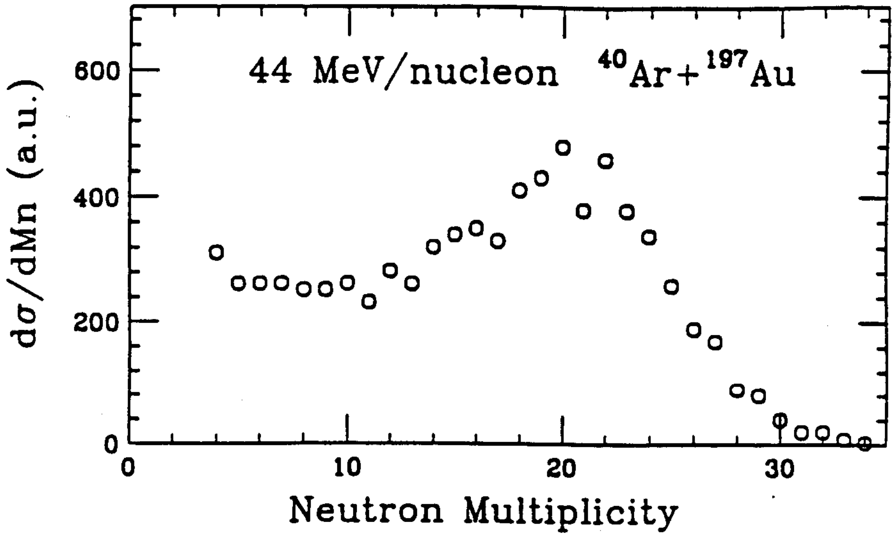

Fig. II.6: Multiplicity distributions of neutrons from the reaction of 2GeV protons (top) and 44MeV/u ^{40}Ar (bottom) with a ^{197}Au target [Pie93]. The available total excitation energies are E^*_{tot} = 1.98 GeV and 1.46 GeV, and the neutron detection efficiencies are $\bar{\varepsilon}$ = 0.6 and 0.8, respectively.

tiplicity provides a measure of dissipated energy and impact parameter superior to experimental observables associated with other particles. Its sensitivity can be increased by using a combination of multiplicity and total kinetic energy of the neutrons emitted in a collision. This latter quantity can be inferred from the "prompt response" signal of the neutron calorimeter. An evaluation of its usefulness in a quantitative study will have to await further experimental evaluation, one of the tasks to be accomplished with the *SuperBall* calorimeter.

III. Design Requirements and Characteristics of Neutron Calorimeters

In the preceding section, the uniqueness and power of the neutron multiplicity observable as indicator of the energy converted into intrinsic excitation energy of a heavy-ion reaction system has been illustrated. The following will present the rationale for the particular design of the *SuperBall* calorimeter, a five-segment liquid-scintillator detector.

In order to measure the important multiplicity observable, one needs to count any and all of a potentially large number of neutrons, up to m $\sim$ 100, which are all emitted simultaneously in a reaction event, with angular and energy distributions determined by the kinematics and the internal excitation of the various emitters. A heavy-ion reaction can produce both, fast-moving projectile-like fragments and remnants of the target nucleus, which are almost at rest in the target, with broad excitation energy spectra. While neutrons emitted from the fast PLF's in flight will be focused into a narrow cone about the direction of flight of the PLF, neutrons evaporated from a slow TLF have an almost isotropic angular distribution. Efficient neutron counting, hence, requires a detector that covers the entire solid angle, has a very low threshold for neutron detection and can stop even very fast neutrons. Since hydrogen-rich, organic scintillators have a high stopping power, 4π liquid-scintillator detectors appear to be good candidates for an efficient detector design.

The cross sections for neutron interactions are very important quantities for the detector design. On the top of Fig. III.1, the cross sections for elastic scattering on hydrogen and for elastic and inelastic scattering on carbon are plotted *vs* neutron kinetic energy [Del76]. One observes that, while at low energies ($E_n \leq 10$ MeV), the elastic n-p cross section dominates, the elastic n-C cross section becomes more and more dominant above 10 MeV. For $E_n \geq 100$ MeV, inelastic n-C cross sections are largest. It is noteworthy that (n,p), (n,α), or (n,npα) neutron capture reactions on C, like elastic n-p scattering, occur "promptly", one a ~ 100 ns time scale, with respect to the injection of the neutrons into the active detector volume. Furthermore, in the former two of these reactions, neutrons are captured promptly, i.e., in one reaction step, while neutrons can undergo many successive elastic-scattering processes leading only to a moderation and eventual thermalization of the neutrons, which will subsequently diffuse through the scintillator. The lower portion of Fig. III.1 shows the actual free path $\lambda(E_n)$ of a neutron in a commercially available organic scintillator liquid (BICRON BC-521), plotted *vs* neutron energy E_n. An efficient detector should have a scintillation layer of a thickness of several times $\lambda(E_n)$, for the largest neutron energies of interest. For heavy-ion reactions at Fermi energies, a typical high neutron energy is of the order of $E_n \sim 100$ MeV, for intermediate energies, neutron energies of several hundreds of MeV would be of interest. Therefore, a highly efficient neutron calorimeter useful for such reactions should have a scintillation layer thickness of (1-2) m. Because of the kinematics of the heavy-ion reactions of interest, the highest neutron energies occur at forward angles. This feature suggests a segmented calorimeter design with forward segments that have a thicker scintillator layer than the backward segments. For this purpose, the calorimeter segmentation could be rather coarse, i.e., a few segments would suffice.

The moderation and subsequent diffusion and capture processes are realistically simulated by a Monte Carlo computer code DENIS [Poi74], modified [Pad89] for the particular application to heavy-ion reactions. Fig. III.2 illustrates the time dependence of the energy moderation process for a particular scintillator (National Diagnostics ND-309).

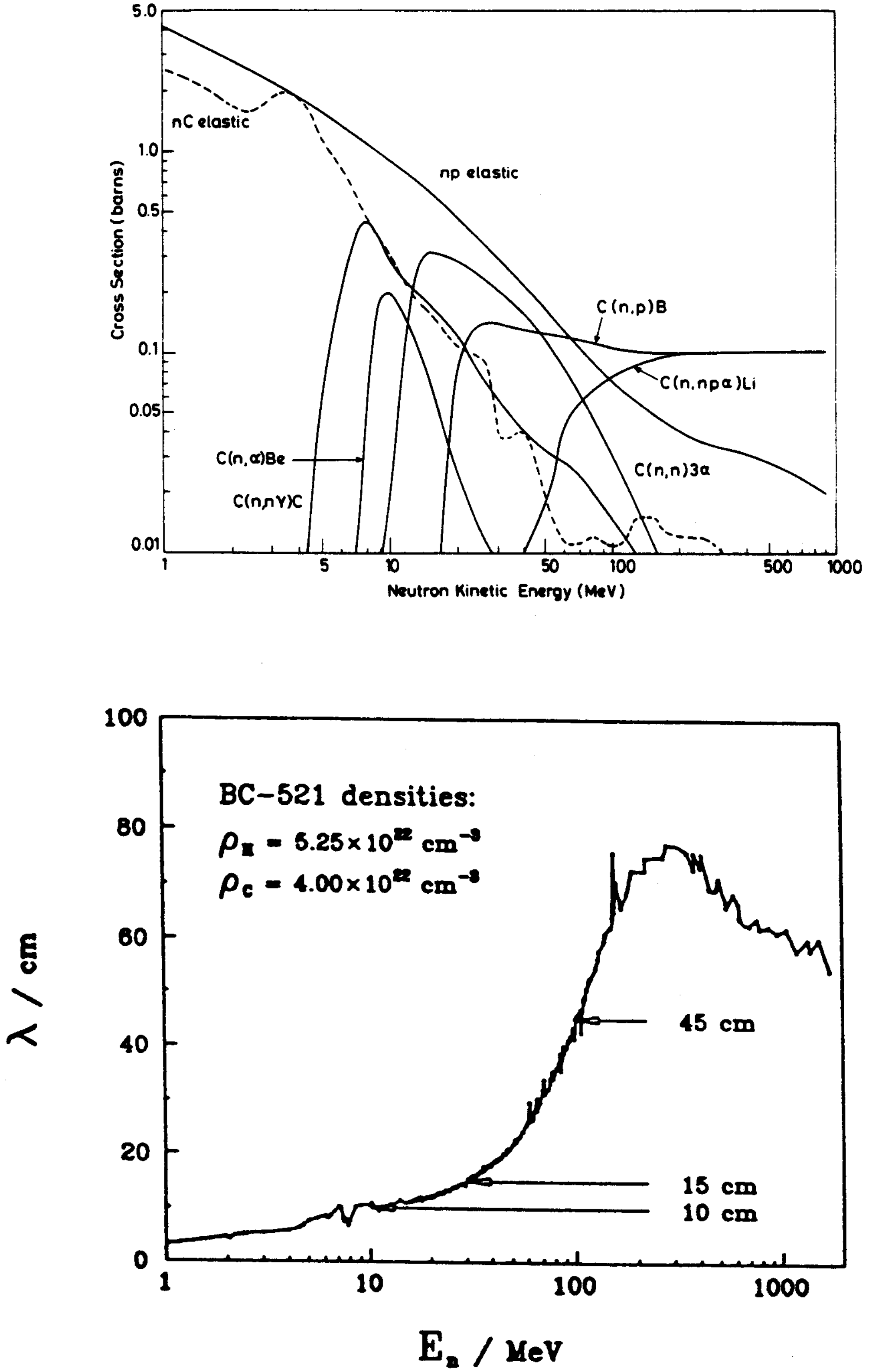

Fig. III.1: The cross sections for elastic scattering on hydrogen and for elastic and inelastic scattering on carbon are plotted *vs* neutron kinetic energy E_n [Del76] (top panel). Mean free path $\lambda(E_n)$ of a neutron in a commercially available organic scintillator liquid (BICRON BC-521) is plotted *vs* neutron energy E_n (bottom panel).

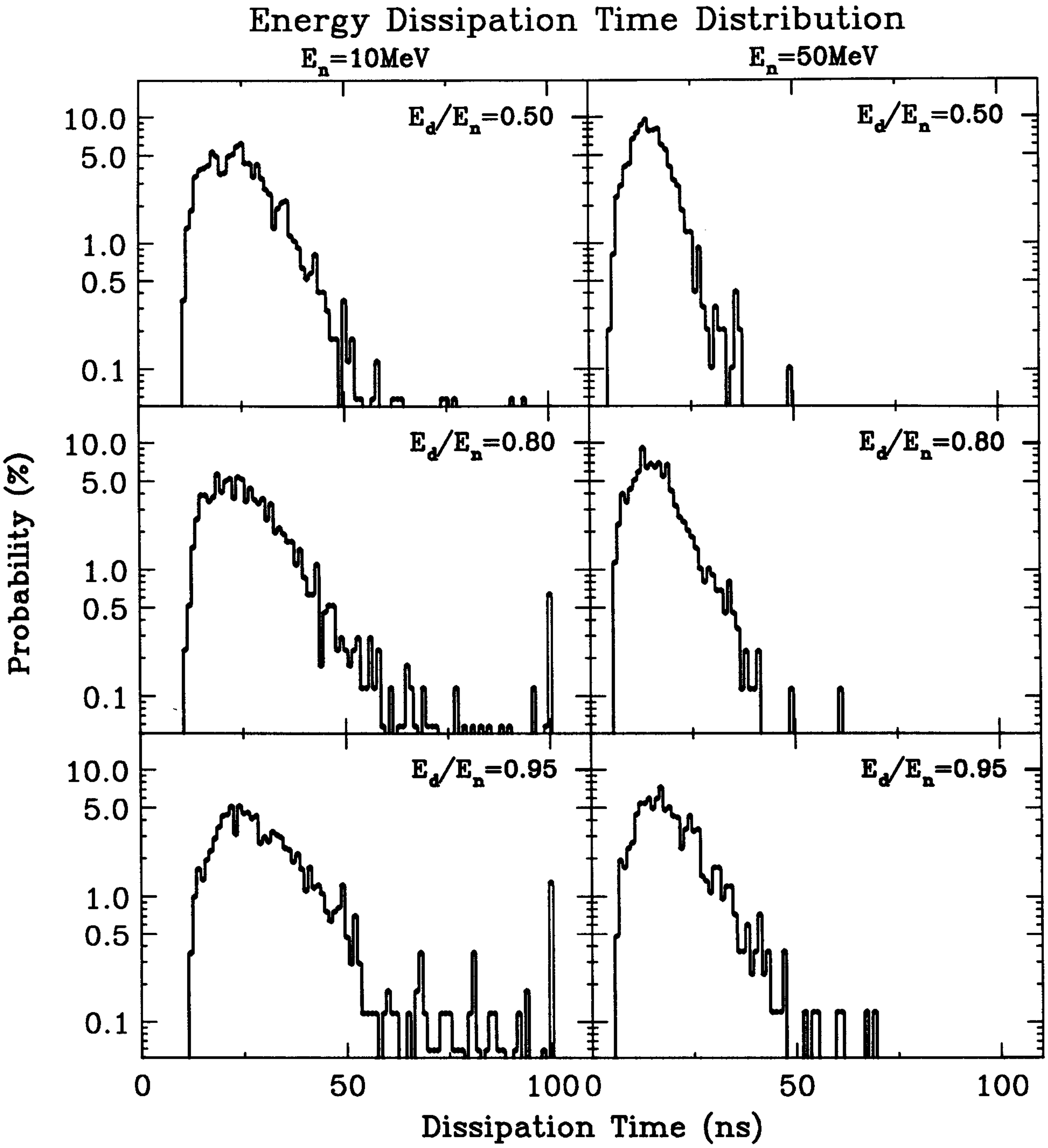

Fig. III.2: Theoretical distributions of the time needed for a neutron of initially E_n = 10 MeV (left) or E_n = 50 MeV (right) to dissipate various fractions E_d/ E_n of the initial energy.

Here, the unnormalized probability is plotted *vs* the time it takes a neutron to dissipate a fraction E_d/E_n = 50%, 80%, and 95% of its initial kinetic energy, for E_n = 10 and 50 MeV. This figure demonstrates that the moderation process is essentially concluded within 50 ns after injection of the neutron into the scintillator, after which a neutron has lost its kinetic energy. For the relatively low neutron energies illustrated in Fig. III.2, the energy is released almost entirely in n-p elastic collisions. Knowing the scintillator response to protons, it is possible to deduce the kinetic energy of the neutron from the corresponding "prompt" scintillation flash, although the relation is usually non-linear. If several neutrons are slowed down simultaneously within the scintillator, the scintillator light output will reflect the total kinetic energy of all neutrons transferred to the scintillator. For higher neutron energies, however, the situation becomes somewhat more complicated, as other processes, in particular n-C scattering and reactions, compete effectively with n-p scattering. In practice, this effect leads to a deterioration of the neutron kinetic-energy resolution afforded by the light-output signal.

Neutrons undergoing reactions on carbon with charged-particle production are associated with scintillation processes that are somewhat different from that of elastic n-p scattering. This is so, because of the different energy spectra of the charged particles, whose recoil into the scintillator generates the scintillation light proper. This is an effect that has to be taken into account in the interpretation of the scintillation light output response occurring promptly in the above sense. In practice, such a requirement can be fulfilled with scintillators whose light response has several components activated with different probabilities by different particles, allowing for particle identification, e.g., by pulse-shape discrimination. Of course, in order to measure the neutron multiplicity accurately, multiple hits of a detector element by neutrons that can lead to event mixing have to be avoided in such a procedure, requiring a highly segmented (4π) detector. To accommodate neutron multiplicities of the order of m ~ 100, occurring in heavy-ion reactions already at Fermi energies, a detector, based on this principle of a measurement of the "prompt" scintillator response to the recoiling secondary charged particles, has to have several hundred segments. Each of these independently operated segments would have to have a scintillator thickness of 1-2 m. A cost analysis shows that this would be a very expensive proposition and, consequently, this detection principle has not been followed in the design of the *SuperBall,* although the prompt response of the scintillator to the neutron moderation process can provide a useful auxiliary signal.

Instead, the principle of operation of the *SuperBall* is based on the delayed response of Gd-loaded liquid scintillator to neutrons, a principle known [Div58,60, Poi74] since long and, more recently, realized [Jah83, Gal90, Pad91] in several detector applications to heavy-ion studies. It allowed the *SuperBall* to be constructed as a liquid-scintillator detector with only a few tank segments, each carrying a number of photomultipliers attached to the walls of the segment. The delayed scintillator response to neutrons is due to the γ-rays following the delayed capture of thermalized neutrons, mainly by the Gd component of the doped scintillator, but to a lesser extent also by its hydrogen content. The Gd isotopes have a very high cross section ($\sim 10^3$ b) for thermal-neutron capture. This capture occurs after the initial fast moderation of the neutrons via multi-scattering processes and some longer period of slow neutron diffusion through the scintillator volume.

Fig. III.3 shows the theoretical capture time distribution for a neutron, plotted *vs* the time elapsed since the injection of the neutron into the scintillator. It corresponds to a particular scintillator (National Diagnostics ND-309) with a Gd concentration of 0.2% by weight. This distribution is well reproduced by the theoretical form

$$f(t) = e^{-\alpha t} \cdot \{t(\beta-\alpha)-1\} + A \cdot e^{-\beta t} \qquad \text{(III.1)}$$

where α , β, and A are constants characterizing the scintillator material. Obviously, this distribution peaks at capture times of the order of 10 μs, but extends further over tens of microseconds, reflecting the time scale of the diffusion process. Hence, a neutron will be delayed statistically over this time scale, before it is captured by a Gd nucleus. The cascade of γ-rays following the capture of a neutron consists of mainly two or three γ-rays, with a total energy of approximately 8.5 MeV. When these γ-rays interact with the scintil-

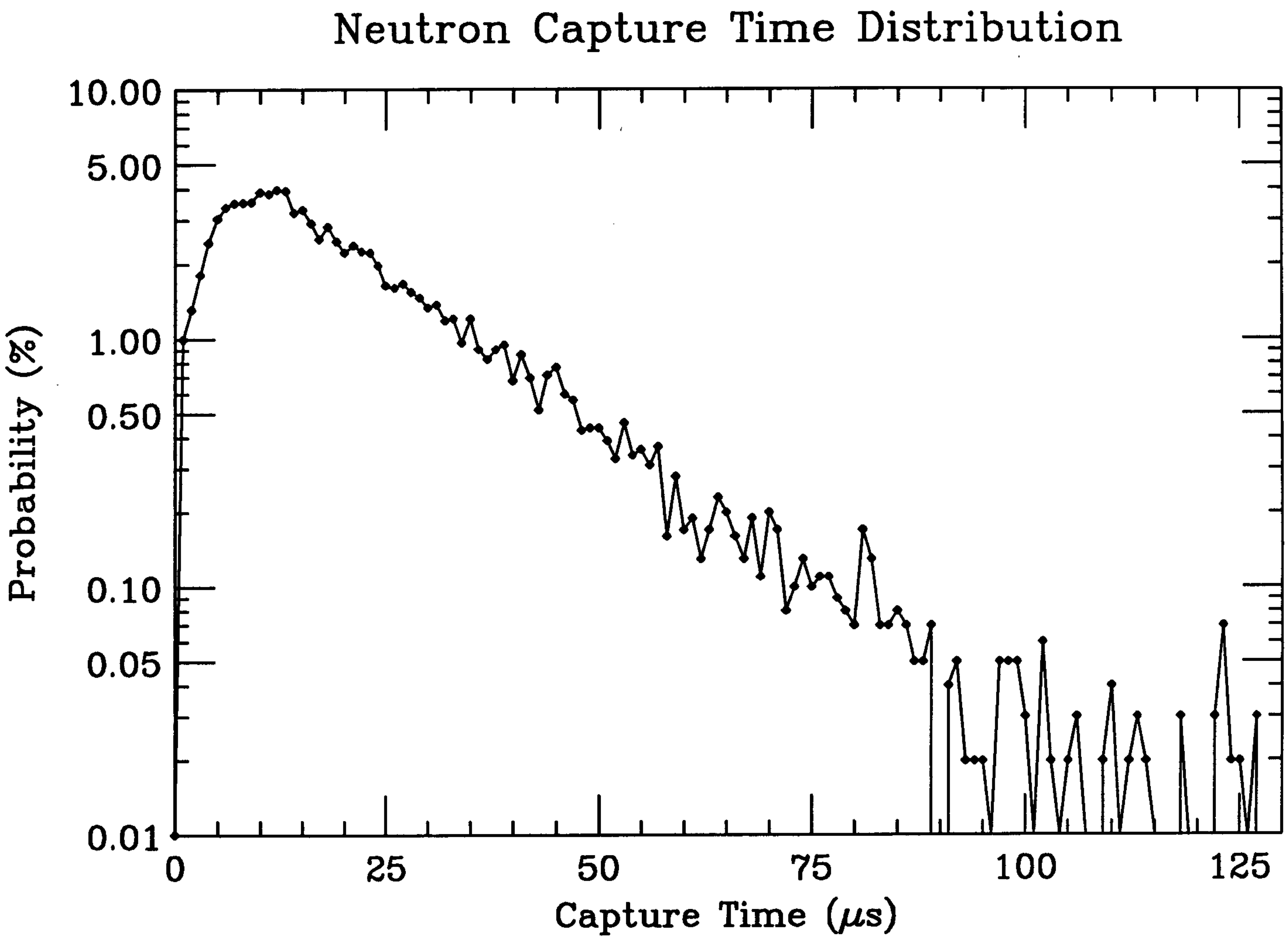

Fig. III.3: Neutron capture time distribution calculated with the Monte Carlo simulation code DENIS.

lator, a scintillation light flash is produced, which is essentially in coincidence with the capture event but statistically delayed by significant amounts of time with respect to the injection of the neutron into the scintillator. These light flashes can be detected using fast photomultipliers mounted to the detector walls and viewing the scintillator inside through windows.

Through the statistical diffusion process, the individual members of an ensemble of neutrons emitted simultaneously in a nuclear reaction are captured at times that are, on average, sufficiently well separated such that the corresponding scintillator light flashes can be counted independently using fast photomultipliers and conventional electronics. Assuming that the multiple-scattering and diffusion trajectories of the various neutrons of the ensemble are independent of each other, the capture time (t_k) distribution of the kth neutron can be expressed in terms of the single-neutron capture time distribution (cf. eq. III.1) as

$$\frac{dN_k(t_k)}{dt_k} = f(t_k) \cdot k \cdot \sum_{n \geq k} \binom{n}{k} P(n) \cdot \left[\int_0^{t_k} dt f(t) \right]^{k-1} \cdot \left[\int_{t_k}^{T} dt' f(t') \right]^{n-k} \qquad \text{(III.2)}$$

where T is the duration of the counting gate accepting neutron capture events and $P(n)$ is the observed multiplicity distribution. The product of $f(t_k)$ and the first k-1 integrals in eq. III.2 result from the requirement that k-1 specified neutrons ($i=1,..., k$-1) are captured at times $t_i \leq t_k$, while the remaining n-k integral factors represent the probability that neutrons ($i=k+1,...,n$) are captured at $t_k < t_i \leq T$. The binomial factor accounts for the different possibilities of selecting k out of n neutrons.

In order to detect all captures associated with a heavy-ion reaction in the target, the counting electronics has to be kept ready to accept neutron capture events for approximately 50 to 100 μs, for the example illustrated in Fig. III.2 making the detector inherently slow. The higher the Gd concentration of the scintillator, the earlier the diffusion process of a neutron will terminate in a capture process and the faster the detector will be able to count. However, since the microscopic deadtime of the detector associated with the detection of a single capture event is finite, the average neutron diffusion preceding capture has to last a certain minimum time, in order to prevent significant counting losses due to event overlap ("pileup"). To reduce such losses to less than one percent limits the practical Gd concentrations to a few times 10^{-3} by weight.

The long calorimeter deadtimes referred to above are, of course, disadvantageous in certain applications. It is important to realize, however, that these very long detector deadtimes can be circumvented by running the calorimeter in a different, faster mode, giving up the multiplicity measurement, for a portion of the total experiment time. Since the multiplicity of evaporated neutrons is correlated with their kinetic-energy spectrum, the measurements of these two observables are, to a certain extent, equivalent. Hence, one can gather pertinent information also from a measurement with the calorimeter run in a "fast" mode, where only the prompt light output is recorded for each event. In this mode, the calorimeter deadtime is very small, in the limit only of the order of 50-100 ns. However, a careful calibration measurement of the prompt light output is required with the calorimeter driven in its normal, "slow" mode.

In order to arrive at an efficient calorimeter design, various simulation calculations were performed. The total detection probability $P(E_n)$ of the detector can be expressed as an integral

$$P(E_n) = \int d\Omega d^3\vec{r} d^3\vec{r}' \sigma(E_n, \Omega) \cdot P_{capt}(E_n, \Omega, \vec{r}) \cdot A_\gamma(\vec{r}, \vec{r}') \cdot L(\vec{r}') \qquad \text{(III.2)}$$

over the products of angular distribution $\sigma(E_n, \Omega)$ of the neutrons, their capture probability $P_{capt}(E_n, \Omega, \vec{r})$ at position $\vec{r}$, which depends on the neutron velocity vector or equivalent quantities, the interaction probability $A_\gamma(\vec{r}, \vec{r}')$ of γ-rays at position $\vec{r}'$, having propagated from the capture site $\vec{r}$ to $\vec{r}'$, and the light collection efficiency $L(\vec{r}')$ for light generated at the scintillation site $\vec{r}'$. In simulation calculations performed in the context of the detector design, different neutron angular distribution $\sigma(E_n, \Omega)$ were assumed, as determined by the different reaction scenarios considered. Capture and γ-ray interaction probabilities were simulated employing the code DENIS [Poi74]. Light losses were assumed to be negligible, in most of these calculations. However, calculations performed [Zha93] to determine suitable numbers and placements on the detector tank segments of photomultipliers for the detection of the scintillation light, included transmission through the liquid, as well as absorption and reflection at the inner surfaces of the tanks.

A schematic sketch of the finally adopted, optimum design for the *SuperBall* is given in Fig. III.4, showing a cross section of the detector, with its internal scattering chamber housing an array of charged-particle detectors (MSU *Miniball*) and attached to the horizontal beam entrance and exit tubes, also shown in this figure. The *SuperBall* detector has five individual scintillator-filled segments, which are rotationally symmetric about the z (beam) axis. The boundaries of the tank segments are defined by radial lines intersecting at the target position. There are gaps of approximately 1” width between two adjacent segments. There is ample space in the center of the detector for a cylindrical (130 cm by 91 cm diameter) scattering chamber with hemispherical end flanges containing the target. Beam entrance is on the left (backward scattering angles), hence, the smaller thickness (102 cm) of the segments on the left *vs*. those of the downstream element (127 cm).

A visual impression of the expected performance of the *SuperBall* neutron calorimeter, fulfilling the basic requirements discussed above, is provided by Fig. III.5. The top parts show each a schematic outline (solid lines) of the *SuperBall* tank segments. The two scatter plots on the top of Fig. III.5 illustrate the distribution $P_{capt}(E_n, \vec{r})$ of capture sites of mono-energetic (left: $E_n = 1$ MeV; right: $E_n = 30$ MeV) neutrons emitted isotropically from a stationary source located in target position. The capture sites plotted in Fig. III.5 were calculated for a thin slice through the detector, parallel to the x-z plane, and integrated over all contributing initial neutron emission angles $\Omega(\theta,\phi)$. At a relatively low energy, e.g., $E_n = 1$ MeV (left panel), the neutrons have a short mean free path (cf. Fig. III.1, bottom panel) and are captured in the vicinity of their entry into the scintillator. Therefore, one observes an outline of the inner cavity and of the radial gaps between the

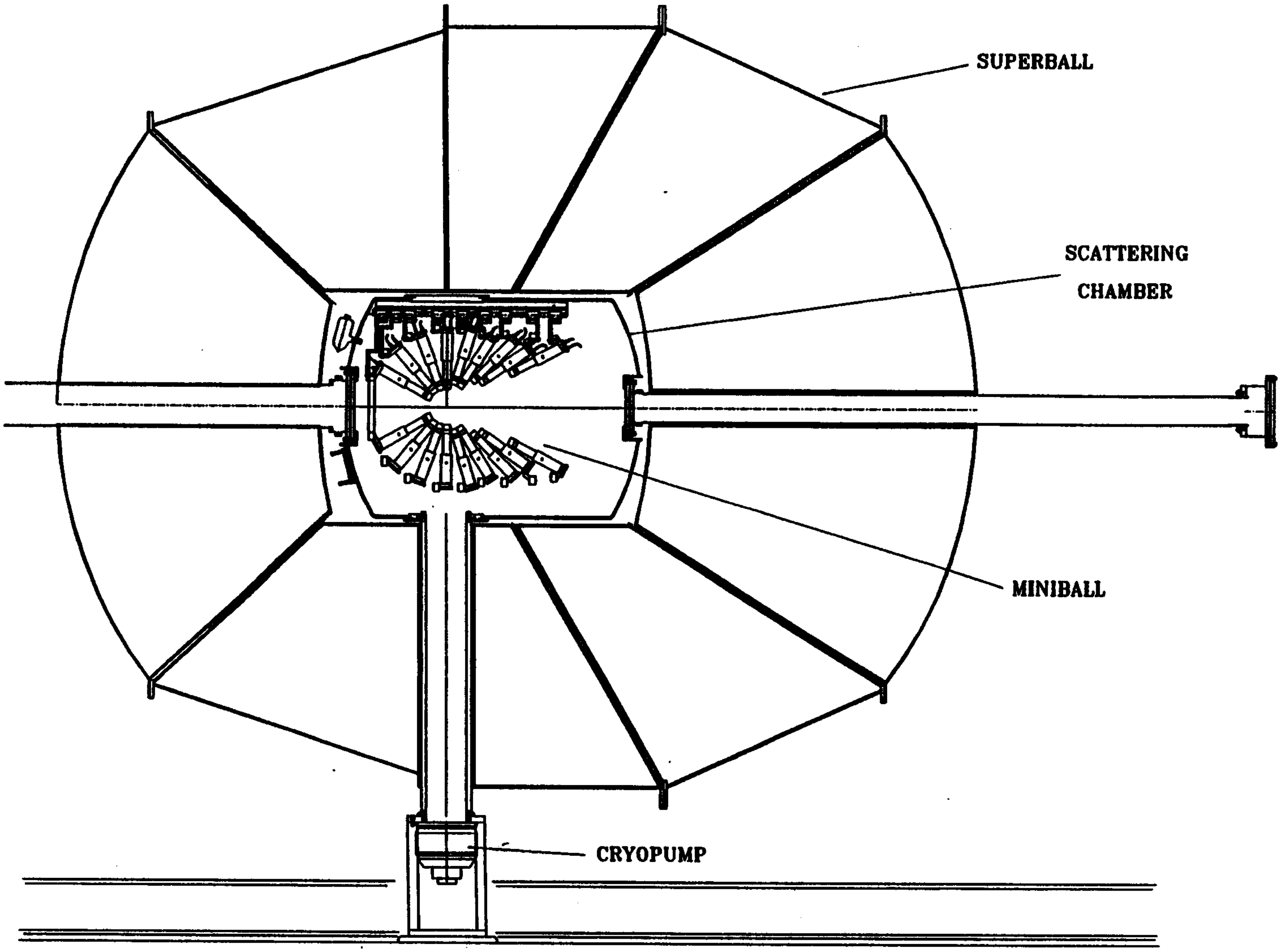
SUPERBALL
SCATTERING CHAMBER
MINIBALL
CRYOPUMP

Fig. III.4: Vertical cross section of the *SuperBall* assembly and scattering chamber with the MSU *Miniball* installed-side view.

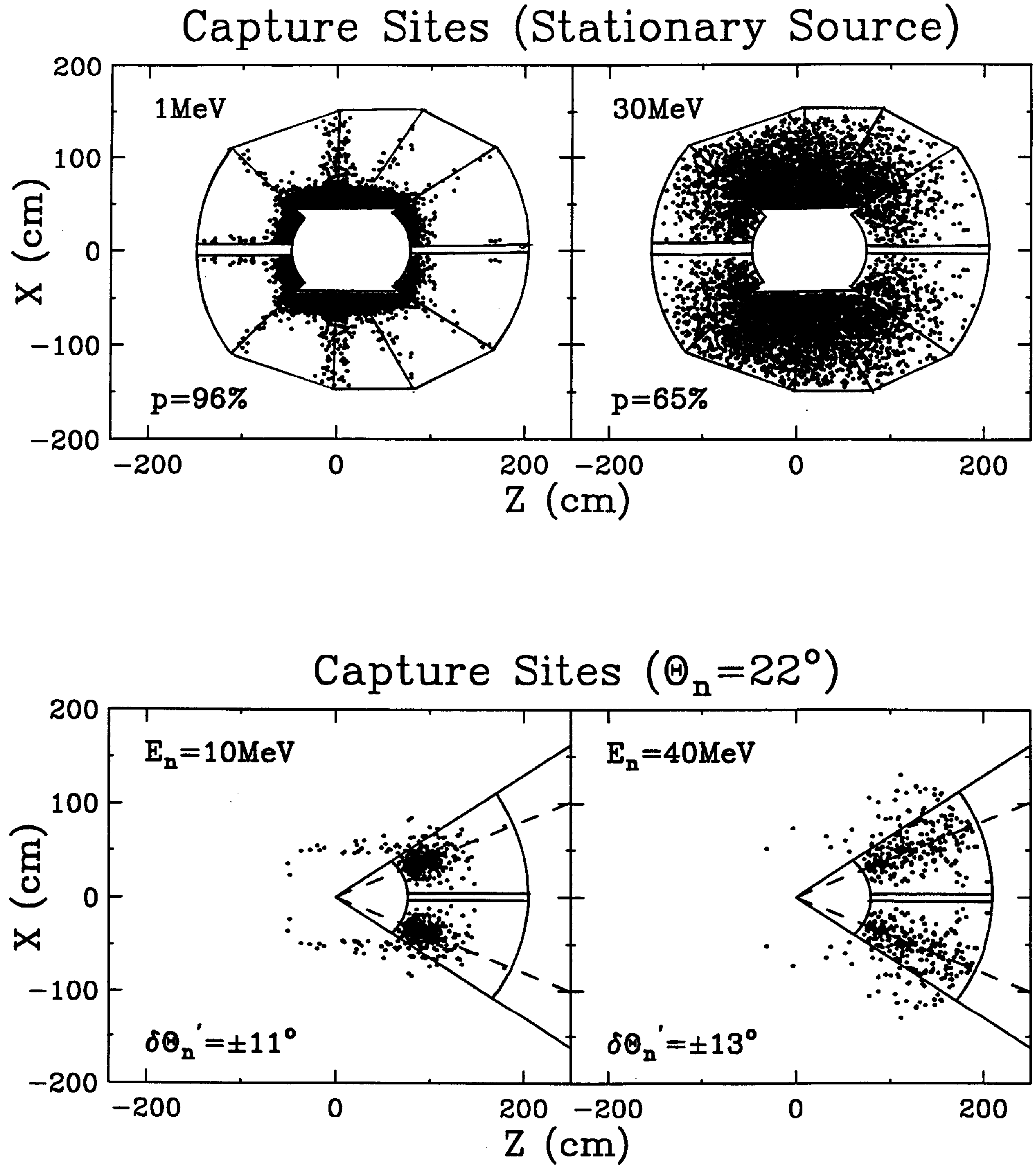

Fig. III.5: Site distribution in the x-z plane where capture in a Gd nucleus occurs, calculated for neutrons of E_n = 1 MeV (upper left) and E_n = 30 MeV (upper right). In the distribution shown in the upper left panel, the internal scattering chamber, the gaps between the tank segments, as well as the beam and ancillary access channels are outlined. The bottom panels show the capture site distributions for neutrons of E_n = 10 MeV (left) or E_n = 40 MeV (right), with initial emission angle of θ_n = 22° (dashed lines) with respect to the beam (z) axis. The forward *SuperBall* tank is outlined by the solid lines.

individual tank segments. Most of the low-energy neutrons are stopped and captured in the scintillator volume, leading to a detection probability of p = 0.96. The upper right panel of Fig. III.5 illustrates the difficulty to stop high-energy neutrons within a finite detector volume. Here, neutron capture sites are plotted for an incident-neutron energy of E_n = 30 MeV. Although the mean free path ($l \approx 0.15$m) is not too large compared to the thickness of the scintillator layer, the neutrons explore the full detector volume, and a significant number of them can actually escape the detector. Therefore, the detection probability for 30-MeV neutrons is reduced to p = 0.65.

It is a result of the forward-peaked angular distribution of the multiple-scattering processes effecting the slowing-down of a neutron, and of the high probability of Gd neutron capture, that the initial direction of flight of that neutron is preserved to a large extent. Of course, the first interaction, in which a neutron loses on average 1/2 of its kinetic energy, is on the original flight path. Further interactions occur with decreasing distance from each other, always favoring the previous direction of flight of the neutron. Once thermalized, the neutron moves during a time period of several tens of ms with a velocity of $v_{therm} \approx 0.2$ cm/μs, in a random-walk-like manner, through the scintillator, until it is captured by a Gd nucleus. Hence, the neutrons never wander too far away off the original flight direction. This feature of the multiple-scattering and diffusion processes is illustrated on the bottom panel of Fig. III.5, depicting again capture sites in the x-z plane, as well as an outline of the most forward detector segment. The data are results of simulation calculations for ensembles of neutrons emitted at a fixed angle of $\theta_n = 22°$ (dashed lines) relative to the beam (z) axis. As can be seen from the calculations for E_n =10 MeV illustrated in the left panel of Fig. III.5, the capture sites cluster in the proximity of the initial direction of flight (dashed lines), with an angular distribution with a mean angle θ_n' slightly larger than the emission angle of $\theta_n = 22°$, a trivial geometrical effect due to the polar coordinate system adopted. The angular distribution is non-Gaussian, with long tails extending to larger angles θ_n'. The standard deviations in scattering angle are of the order of $\delta\theta_n' = 10°$.

The results of simulation calculations for a range of neutron energies are collected in Fig. III.6. Here, the mean orientation angle of the capture-site distribution is plotted *vs* neutron energy, along with the FWHM angle and the standard deviation of the distribution, for an initial emission angle of $\theta_n = 22^\circ$. In the calculations represented in the upper panel of the figure, it was assumed that only a fraction $E_d/E_n = 0.8$ of the initial neutron kinetic energy was dissipated through multiple scattering, whereas the calculations shown at the bottom of this figure correspond to full moderation. These calculations suggest that the original angular distribution is largely preserved and can, in principle, be measured with a neutron detector based on the present principle of operation. A typical angular resolution achievable with such a detector is $\Delta\theta_n' = \pm 10^\circ$. This figure defines the requirements on the detector's position sensitivity, which in the case of the *SuperBall* is realized through angular segmentation. The angular segmentation illustrated by the radial lines in Fig. III.4 conforms to this requirement.

The detection efficiencies of a detector of the geometry schematically illustrated Fig. III.4 and its segments are depicted in Fig. III.7, for neutrons evaporated from a hot emitter moving in beam direction. The fast sources represent excited projectile-like reaction fragments, while the slower sources simulate the corresponding target-like fragments. The neutron energy spectra in the rest frames of the corresponding emitters are assumed to be Maxwell-Boltzmann distributions with the temperature parameters T given in the legend. Realistically high T parameters were assumed at each source kinetic energy. These finite temperature parameters increase the efficiency for neutrons emitted from fast sources, which would otherwise (for $T \approx 0$) escape through the exit beam pipe. The top panel of this figure shows the variation of the total efficiency (probability), whereas the response of the individual detector segments is given in the bottom part of the figure. As expected, the higher the velocity of the emitter, the lower the overall detection efficiency turns out to be. One observes that typical detection efficiencies range from more than 90%, for slow-moving target-like or spectator-type fragments, to below 50%, for highly excited projectile-like fragments with a kinetic energy of 50 MeV per nucleon.

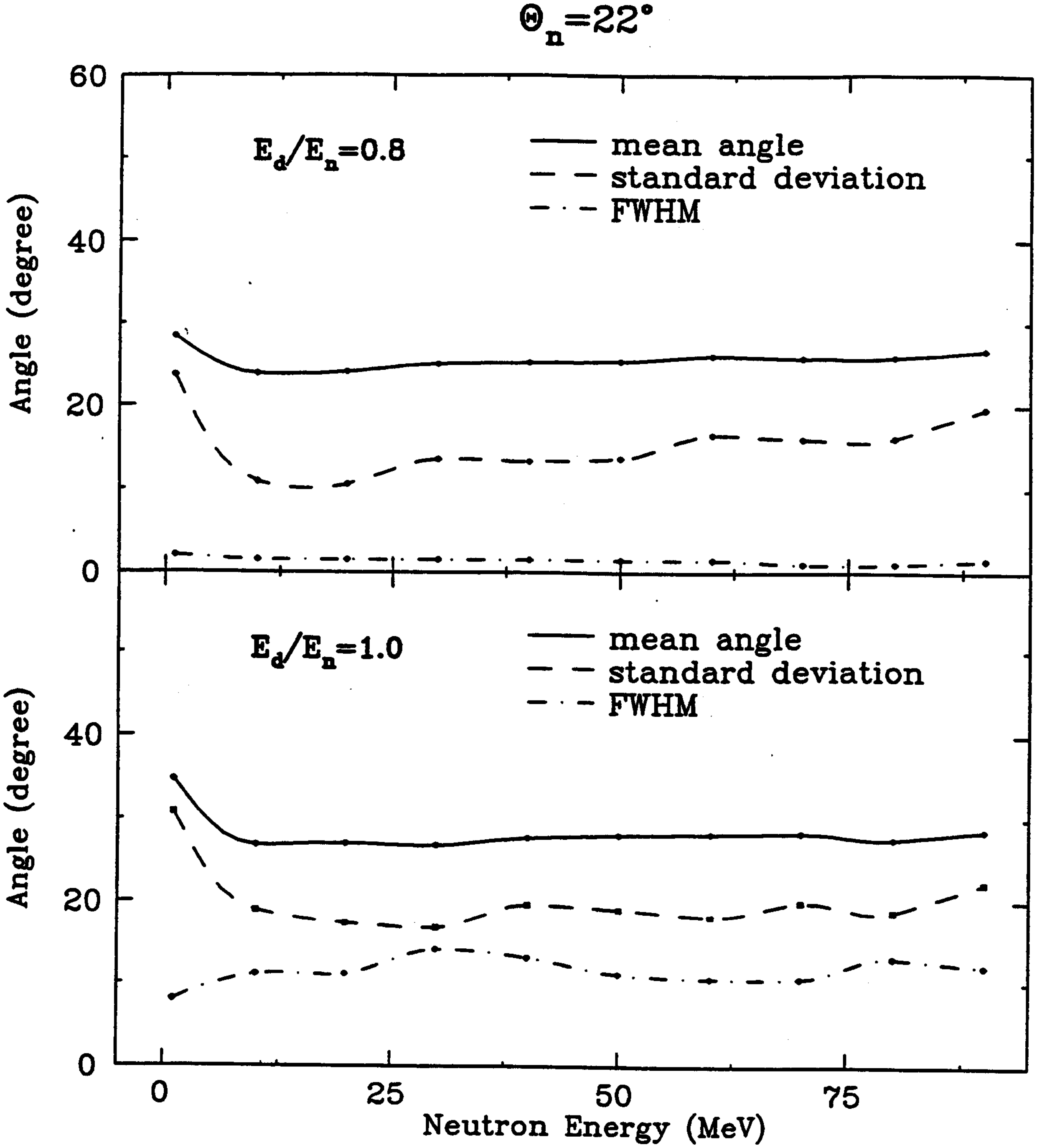

Fig. III.6: Rms angle, standard deviation, and FWHM of straggling angular distribution *vs* initial neutron kinetic energy, calculated for neutrons emitted initially at θ_n = 22° and fractional energy losses of 0.8 (top) and 1.0 (bottom).

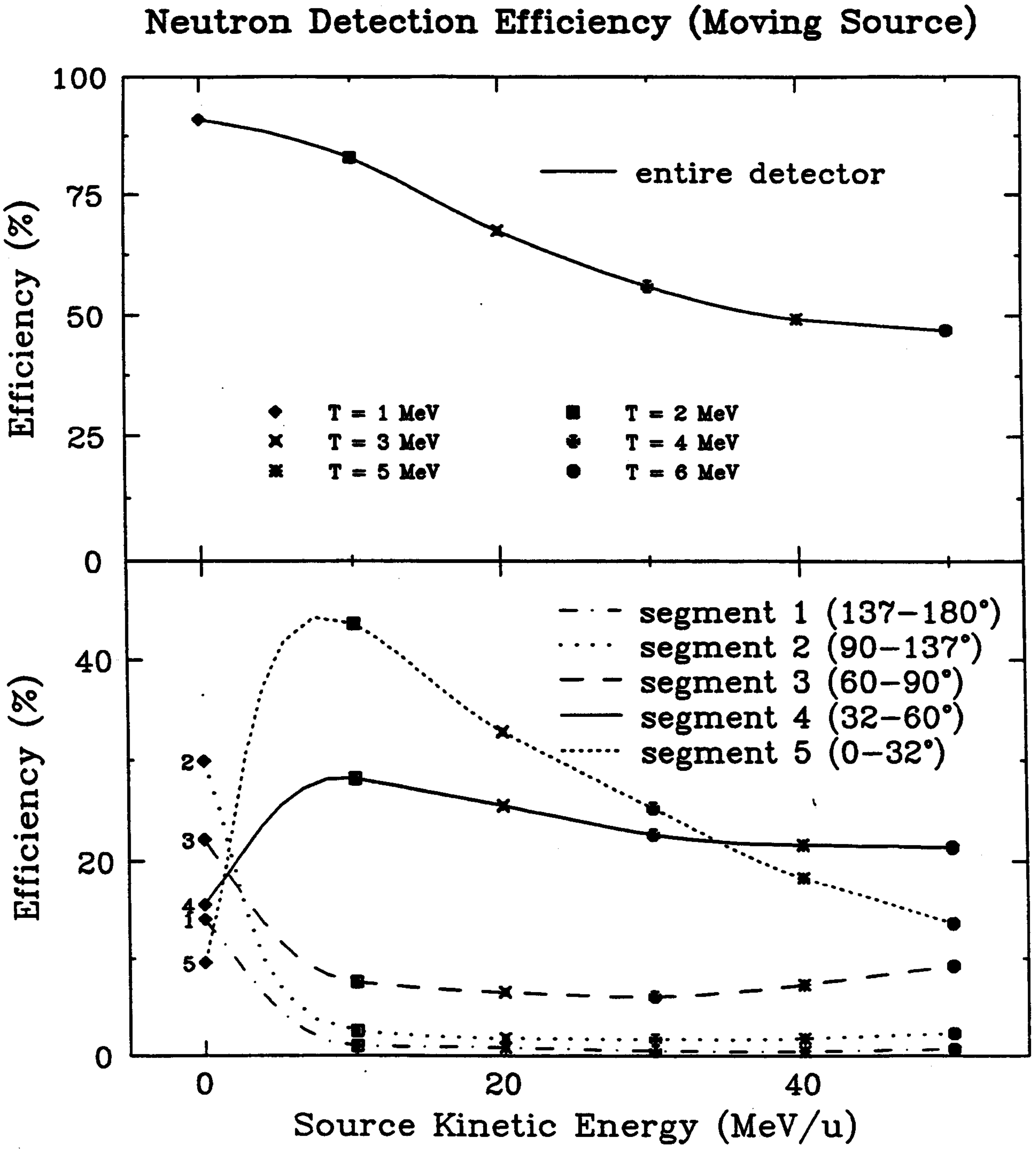

Fig. III.7: Theoretical *SuperBall* detection (capture) efficiency *vs* emitter energy per nucleon, for the entire *SuperBall* (top) and its individual segments (bottom). Maxwell-type neutron spectra with temperature parameters T have been assumed in the emitter frames.

Because of the different degrees of angular "focusing" of the neutrons emitted from sources moving with different velocities, the different detector segments have different effective solid angles and, hence, efficiencies for detecting neutrons from such sources. As seen from the lower panel of Fig. III.7, the *SuperBall* backward segments have a relatively low efficiency for neutrons emitted from any, but very slowly moving sources. The symbols plotted in Fig. III.7 at zero source kinetic energy represent essentially the solid angles of the various tank segments. The forward segments 4 and 5, on the other hand, have reasonably large efficiencies to detect neutrons from fast-moving sources. These differences can be used to deduce information about the kinematics of unknown emitters produced in a heavy-ion reaction.

IV. Mechanical Design

The basic geometry of the final design of the *SuperBall* neutron calorimeter with five individual liquid-scintillator tank segments, as displayed in Fig. III.4, is the result of considerations attempting to optimize versatility and performance for the intended applications in intermediate-energy heavy-ion reactions, under certain cost boundaries ($\lesssim$ \$ 300-400 k). This design was arrived at with the aid of extensive simulations of the detector response to a variety of reaction scenarios, as described briefly in the preceding section. The practical design work was started in September 1991, following the approval of the *SuperBall* project by the U.S. Department of Energy in its University Research Instrumentation Program. The initial design work was carried out in collaboration with Mr. M. J. Fonzi of *Diversified Manufacturing Co.(DMI)*, Lockport, New York until May of 1992. (Later in the year, the collaboration on the *SuperBall* project was dissolved, when it became clear that *DMI* would be unable to manufacture the detector within the budgetary limits of the project.) The final and detail design of the *SuperBall* tanks and interlacing undercarriages was produced by Mr. J.H. Ottarson (*National Superconducting Cyclotron*

Laboratory, Michigan State University, East Lansing, Michigan), who also generated the final engineering drawings.

One important design criterion was that the *SuperBall* should accommodate, in its internal scattering chamber, any of a number of existing 4π charged-particle detector arrays, in order to facilitate a new type of experiment in which all light particles could be measured with full angular coverage. The size of the MSU *Miniball* array, pictured in Fig. III.4 as residing in the *SuperBall* scattering chamber, was used to gauge the minimum dimension of the internal chamber.

In Fig. IV.1, a cross section of the scattering chamber is seen in more detail. It is a cylindrical chamber with dished end caps, with overall dimensions of 130 cm by 91 cm diameter. It has three major parts: One stationary, main chamber ring made of aluminum, on which two removable, dome-like end caps are mounted. These latter caps are made of 1/4" SS304 stainless-steel cylinder sections and spherical dished flanges, connecting to the entrance and exit beam pipes through additional 6" and 4" ISO flanges, respectively. The rolled aluminum (6061) ring has the dimensions of 83.82 cm ID x 88.90 cm OD x 30.48 cm long. It provides mechanical support for all major components of the experimental setup housed by the scattering chamber. It is mounted on an 20.32 cm (8") diameter stainless-steel pipe attached to a steel support structure bolted to the floor of the experimental area. This pipe is connected to the interior of the scattering chamber and is also used as a pumping duct. An 20.32 cm *CIT Cryogenics Cryo-Torr 8F* low-profile cryopump is attached to the pipe, isolated by an 20.32 cm *KEY High Vacuum Products GV-8CP* pneumatic gate valve. The main chamber ring has 4 opposing lateral, 13 cm diameter ports, in addition to the 20.32 cm diameter pumping port on the bottom. Two of these ports are located at angles of $\Delta\theta_n = \pm 15°$ relative to the horizontal, on either side of the main chamber ring. They are used for the feed-through of cables, coolant and counting-gas lines, as well as for other experimental or diagnostic probes. The arrangement is illustrated in Fig. IV.2 showing a cross section through the chamber and an end view of segment 2, again with a multi-detector array inside the chamber. The ports on

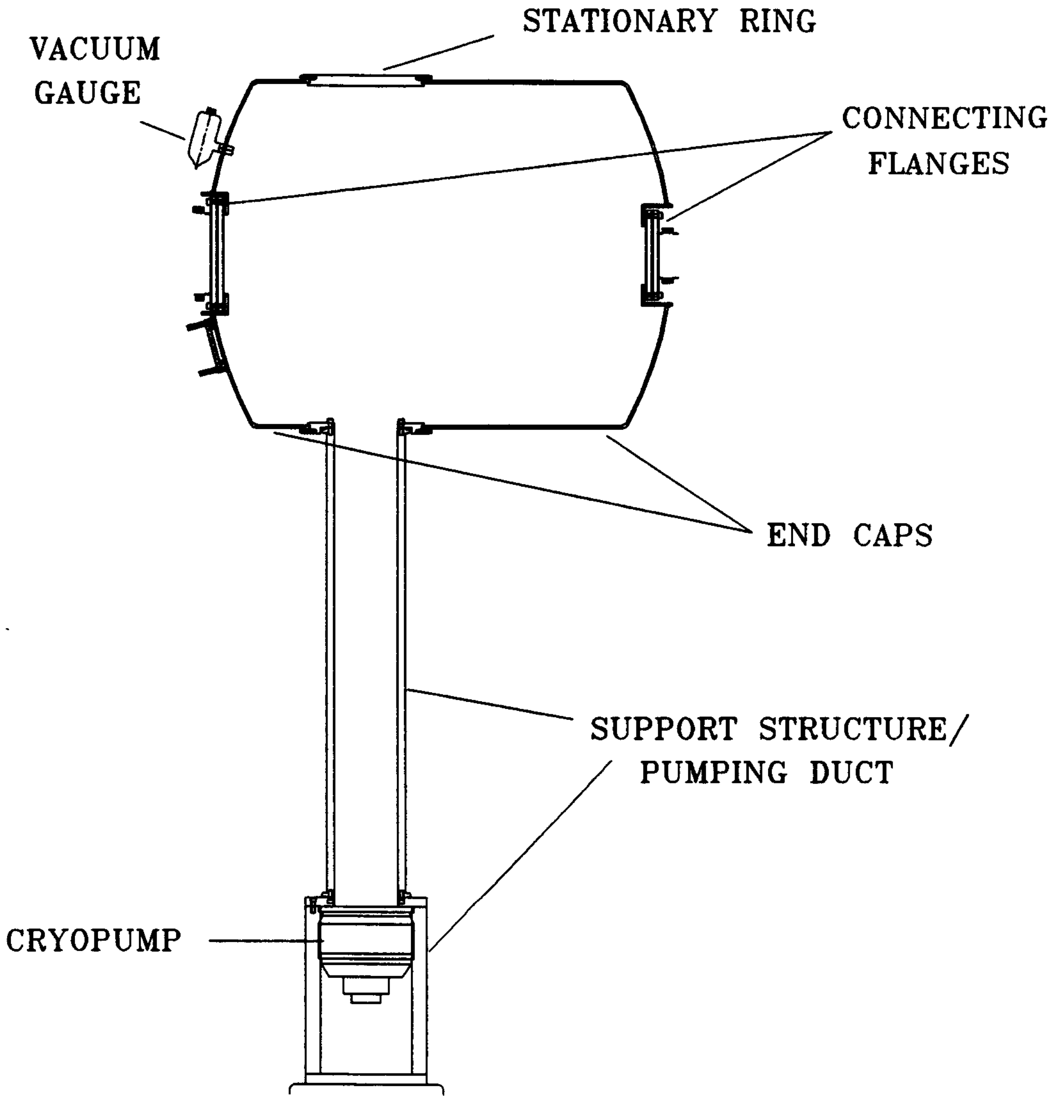
STATIONARY RING
VACUUM GAUGE
CONNECTING FLANGES
END CAPS
SUPPORT STRUCTURE/ PUMPING DUCT
CRYOPUMP

Fig. IV.1: Vertical cross section of the *SuperBall* scattering chamber and of the supporting structure - side view.

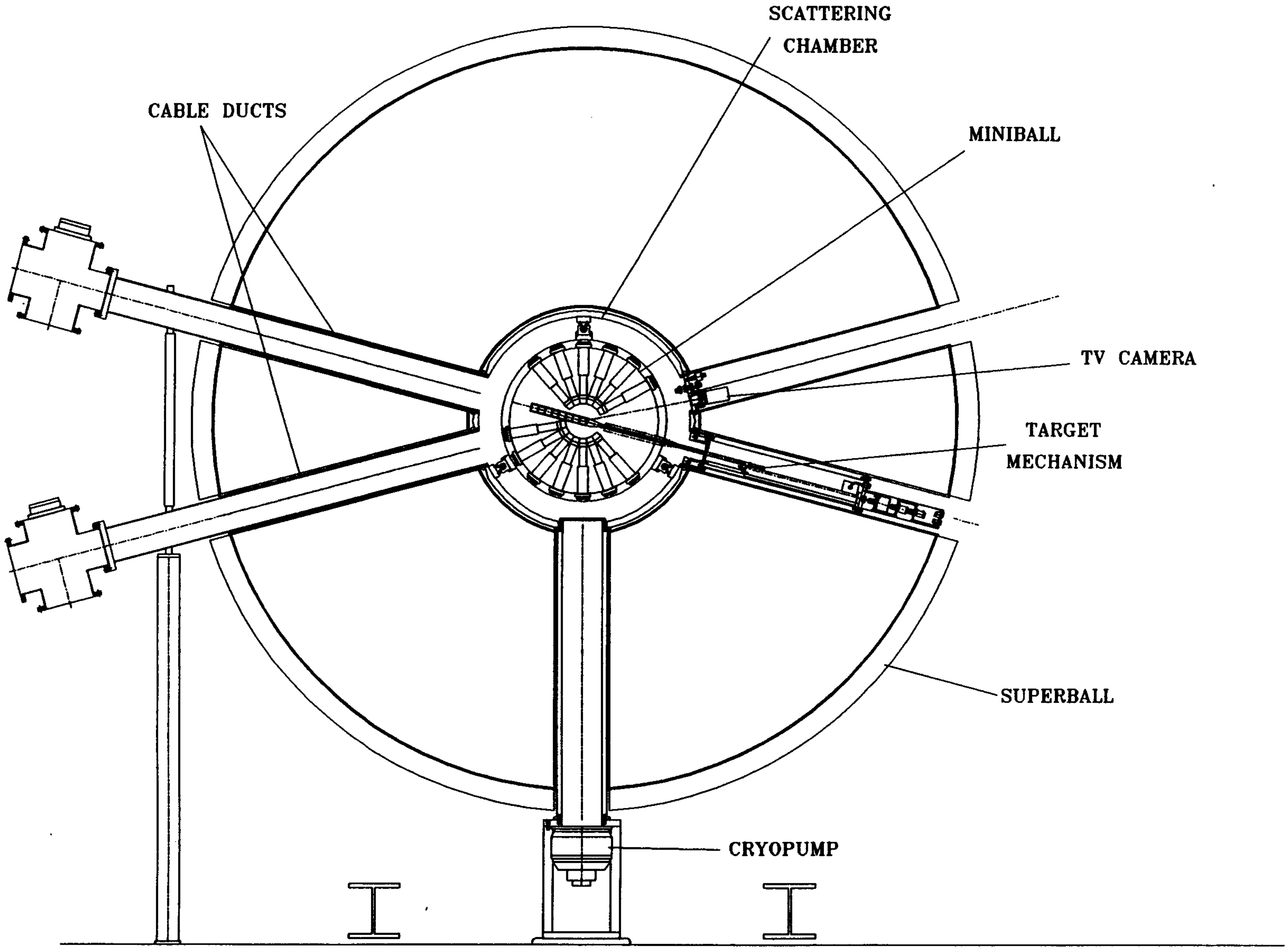
SCATTERING
CHAMBER
CABLE DUCTS
MINIBALL
TV CAMERA
TARGET
MECHANISM
SUPERBALL
CRYOPUMP

Fig. IV.2: Vertical cross section of the *SuperBall* assembly and scattering chamber with the MSU *Miniball* installed - front view.

the left are seen connected to two cable duct pipes, while the two ports on the right-hand side carry various devices, including a target ladder mechanism.

Given the above dimensions of the internal scattering chamber, the overall size of the *SuperBall* calorimeter then follows from the efficiency considerations presented in Section III. The important dimensions of the final *SuperBall* design are collected in Table 1.

The mechanical design of the *SuperBall* is illustrated by the perspective drawing of Fig. IV.3, showing the detector with all segments locked in "docking" configuration, as the detector would be used in a standard experimental setup. In this figure, the beam direction is from left to right. Each of the segments is held by an adjustable support structure mounted on undercarriages with rollers moving on a pair of rails. One of the rails (beam-right) has a planar surface, the other (beam-left) carries triangular guard rails to ensure proper alignment of the segments. To achieve mechanical stability of the tank segments against tilting, the bases of the undercarriages have to be sufficiently long. To still be able to move the tanks closely together, the bases of different tanks have to have different widths and shapes, such that they interlace in the close position. Therefore, the

Table 1: Mechanical-Design Parameters of the *SuperBall* Neutron Calorimeter

	Angular Coverage (degrees)	*Solid Angle (4π sr)*	*Scintillator Thickness (cm)*	*Volume (m^3)*	*Empty Weight (10^3 kg)*
Segment 1	137 -180	0.14	102	1.91	0.48
Segment 2	90 -137	0.34	102	4.25	1.11
Segment 3	60 - 90	0.25	102	3.49	1.10
Segment 4	32 - 60	0.17	102	4.21	1.09
Segment 5	0 - 32	0.08	127	2.46	0.53
Entire Detector	0 -180	0.98		16.31	4.30

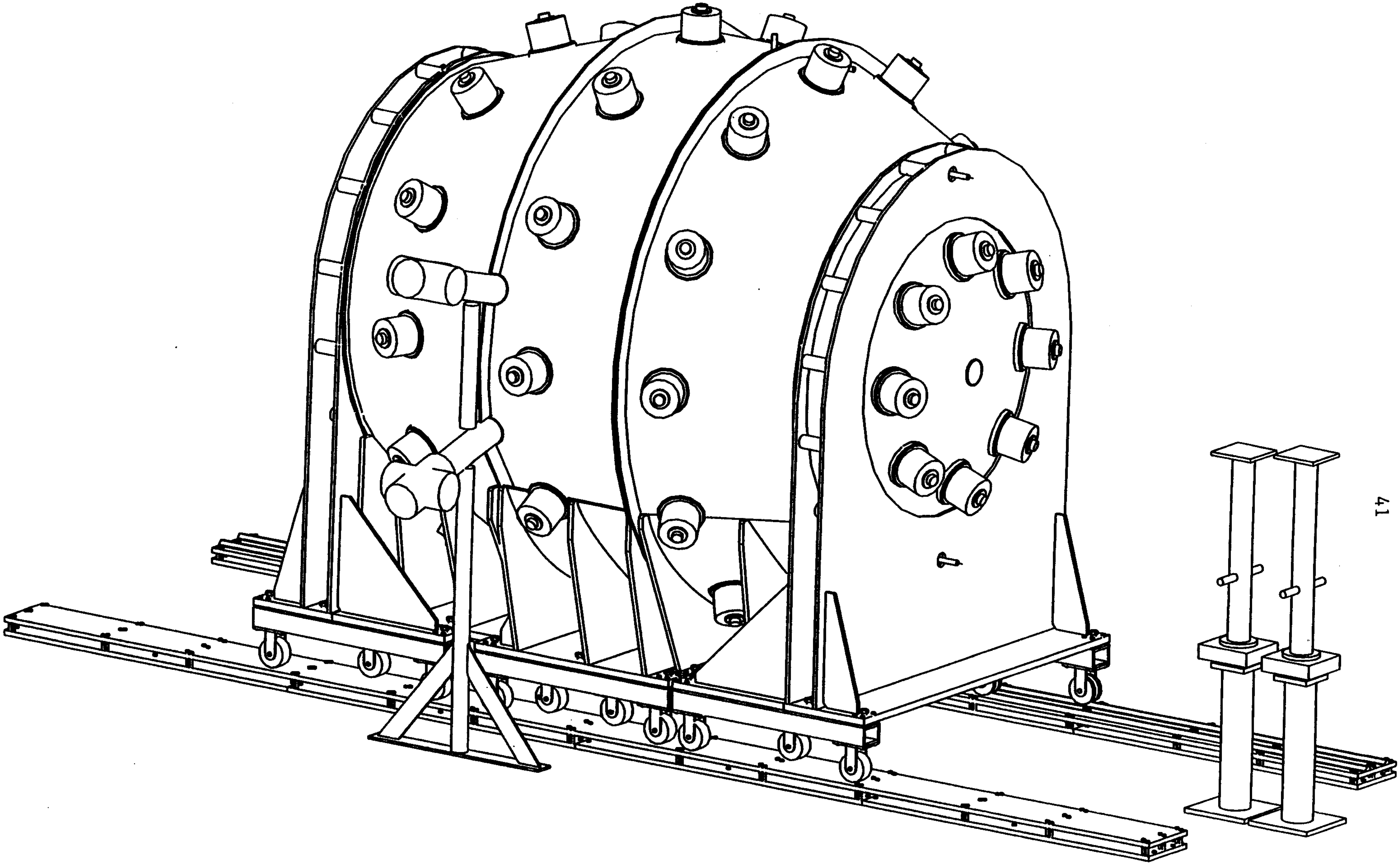

Fig. IV.3: Perspective view of the *SuperBall* assembly in docked, operating configuration.

rails have to be sufficiently wide to accommodate two sets of rollers side by side, and one of them has to carry a pair of guard rails. This is also the reason why the rollers of the tank undercarriages appear staggered in Fig. IV.3 . The dimensions of the two carbon steel rails are 2.54 cm x 35.56 cm x 7.32 m. They are supported each by 28 threaded steel rods, which permit also height adjustment and leveling of the rails.

Fig. IV.4 and Fig. IV.5 depict a horizontal section and a cross section view of the *SuperBall* assembly, respectively, including the most important dimensions. The assembly is 3.88 m long and 3.65 m high. In the horizontal section of Fig. IV.4, one recognizes the tubular inner sections on the left and right, meant to accommodate beam entrance and exit pipes, respectively, and one of each of the two left and right auxiliary duct pipes providing access to the scattering chamber. The circle at the intersection of the radial lines indicates the vertical support and pumping pipe. In Fig. IV.6, one of the end tanks, segment 5, is shown in more detail, both in front (right) and side view (left). Tank segment 1 has a similar design. This tank has approximately the shape of a truncated segment of a sphere which will fit into the conical opening of the adjacent segment 4. The ladder-like structure seen in the side view represents part of the support of this tank and consists of two parallel, vertical 1/2"-thick carbon steel plates attached to the large flange of this tank. The plates are welded together with cylindrical spacers. In addition, two triangular buttresses, welded to the front shell of the segment, form part of the tank support. The whole structure is welded to a rectangular base plate, made of 1"-thick carbon steel and mounted to frame of hollow rectangular steel tubing, which also holds the rollers. Each of the inner tank segments 2-4 is supported from the bottom, by a cradle made of a 1/2"-thick steel "belly band" welded to several vertical steel plates of appropriate shape.

In order to improve the mechanical stability of the shells of some of the circular or conical tank end pieces against deformation that could have been caused by the pressure exerted by the weight of the scintillator inside, tank segments 2 and 3 were reinforced, each by 8 rods of 1/2" diameter stainless steel. The rods were mounted parallel to the symmetry axis of each tank, at half radius, and welded to the shells of these end pieces.

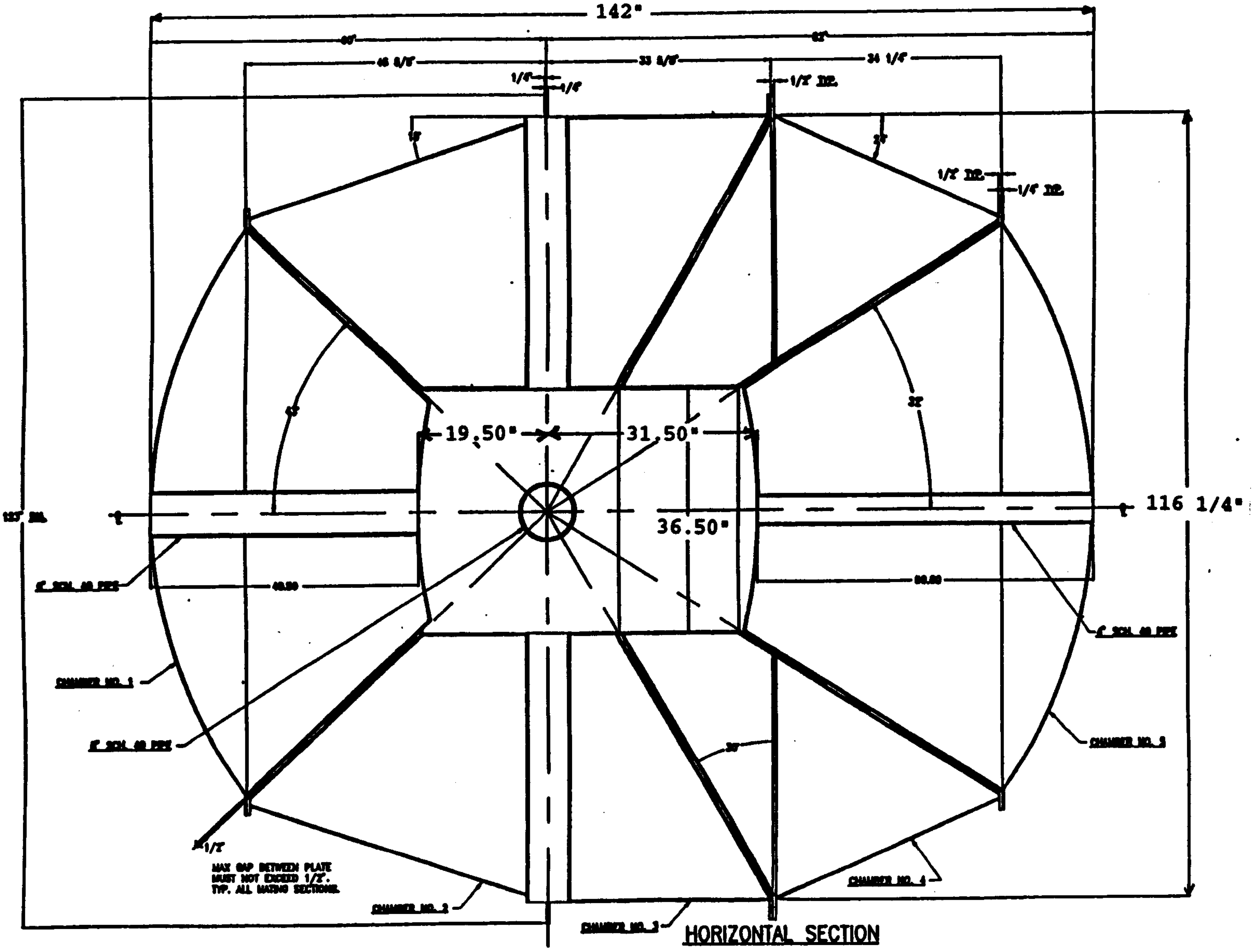
142"
1/4"
1/4"
1/2" TYP.
1/2" TYP.
1/4" TYP.
19.50"
31.50"
36.50"
116 1/4"
1/2"
MAX GAP BETWEEN PLATE
MUST NOT EXCEED 1/2".
TYP. ALL MATING SECTIONS.
CHAMBER NO. 1
CHAMBER NO. 2
CHAMBER NO. 3
CHAMBER NO. 4
CHAMBER NO. 5
HORIZONTAL SECTION

Fig. IV.4: *SuperBall* engineering drawing of a horizontal cross sectional view of docked tank assembly.

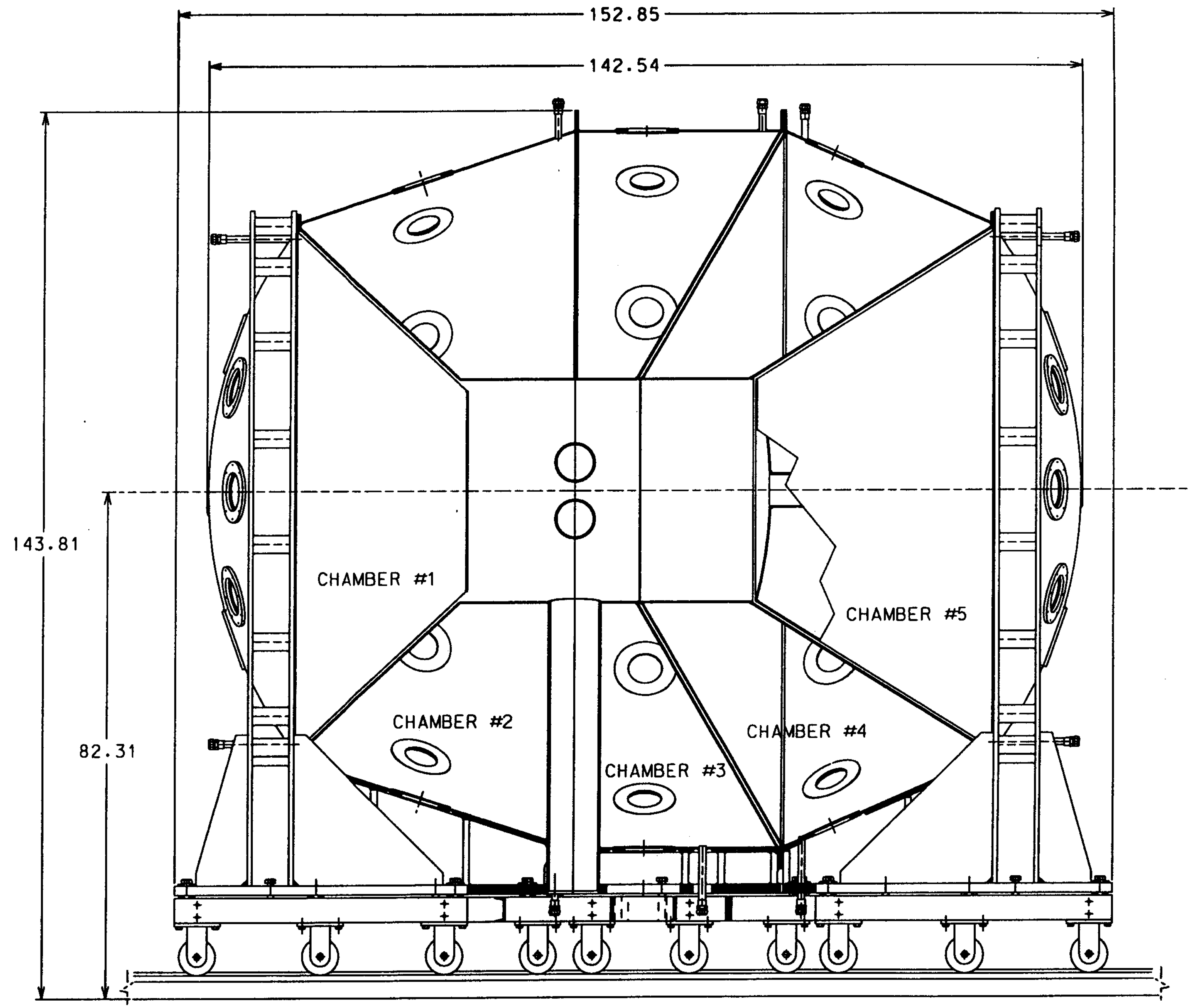
152.85
142.54
143.81
82.31
CHAMBER #1
CHAMBER #2
CHAMBER #3
CHAMBER #4
CHAMBER #5

Fig. IV.5: *SuperBall* engineering drawing of a vertical cross sectional view of docked tank assembly.

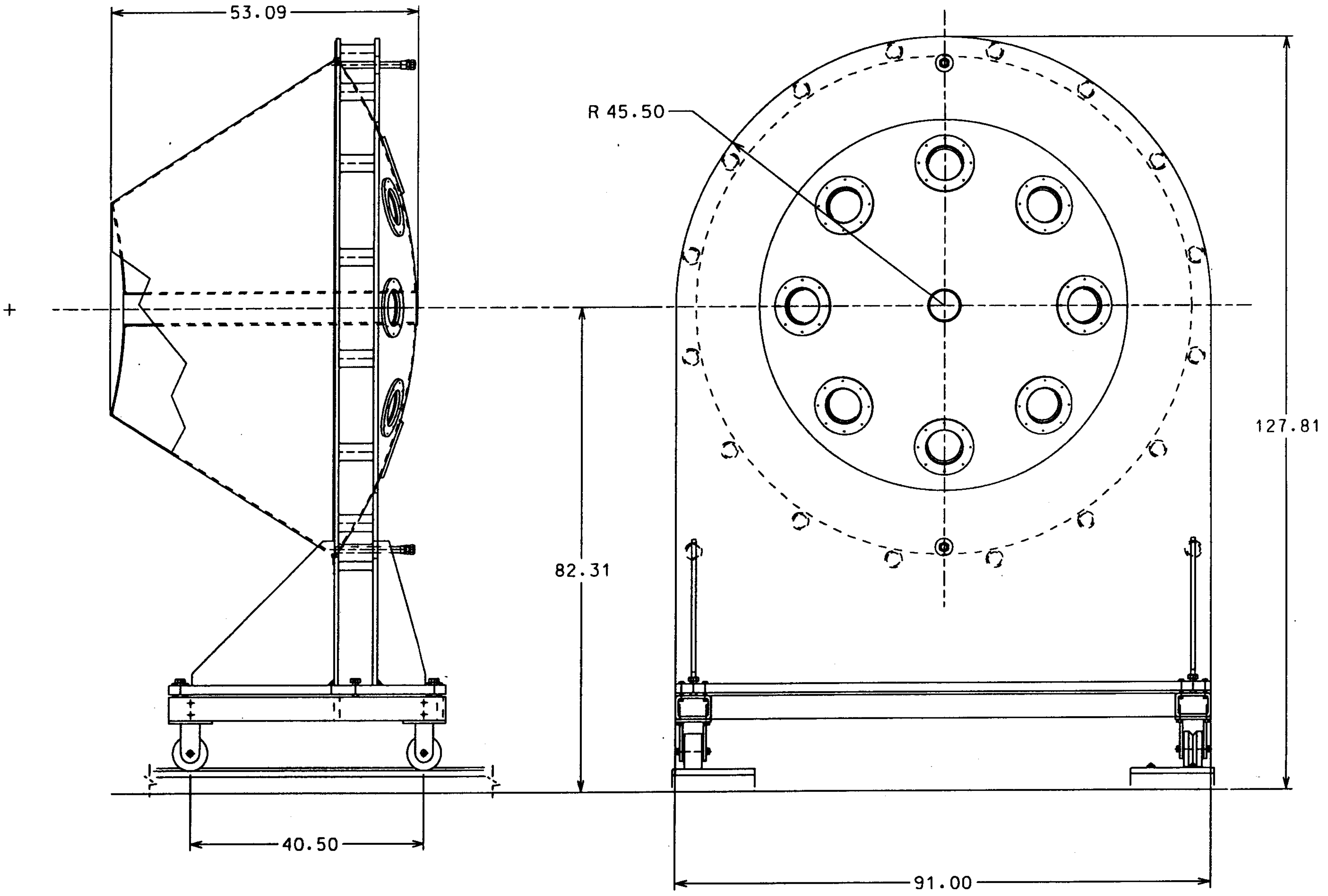
53.09
R 45.50
127.81
82.31
40.50
91.00

Fig. IV.6: *SuperBall* engineering drawing of end and side view of tank segment 5.

Each tank has one stainless-steel inlet and one outlet pipe for the scintillator transfer, close to the lowest and the highest point of the tank, respectively.

Fig. IV.3 shows also the arrangement of 12.7 cm (5") diameter photomultipliers on the different tanks, indicated by the cylindrical aluminum housings with flanges and the bases of the various photomultipliers mounted on the outer tank shells. The two end segments have each 8 photomultipliers, while each of the three inner segments carry 12 photomultipliers, i.e., there are 52 photomultipliers in total. They are attached to the outer shells of the tank segments and view their scintillator-filled interior through window flanges. A vertical cross section of an assembly of such a flange, with photomultiplier and housing, is pictured in Fig. IV.7. At the bottom, this figure shows the stainless-steel window flange, also visible in Fig. IV.7. Each flange holds a ground glass window (1.27 cm (1/2")-thick SW Float, manufactured by *Glass Fab Inc.*), with a Viton O-ring providing the liquid-air seal. The window is pressed against the O-ring by an aluminum collar ring which fits into a recession at the outer periphery of the glass. This way, the collar ring provides no obstacle, if one wanted to slide the photomultiplier sideways, as is useful in the dismounting procedure. Each flange carries also a hermetically sealed aluminum housing can holding the photomultiplier at its socket, with a compressed O-ring seal. The housing can provides additional safety against leakage of scintillator to the outside, in the event that a window should break. The housing cans can be flushed with inert gas (e.g., N_2) to reduce any residual fire hazard. Two tapped holes are provided in the lid of the can to hold gas inlet and outlet tubes. Not shown in Fig. IV.7 is the 14 cm by 13.65 cm diameter *AD-MU-80* magnetic shield cylinder purchased from *Ad-Vance Magnetics Inc.*

In addition to the five tank segments of the *SuperBall*, one approximately cylindrical, 3.672 m by 1.372 m diameter, stainless-steel tank with a volume of ≈ 4.7 m^3 was designed for maintenance and safety reasons. A schematic drawing of the tank is shown in Fig. IV.8. The cylinder is held vertical by a carbon-steel, 3-leg support welded to the lower part of the cylinder. The volume of this maintenance tank is sufficiently large to hold the

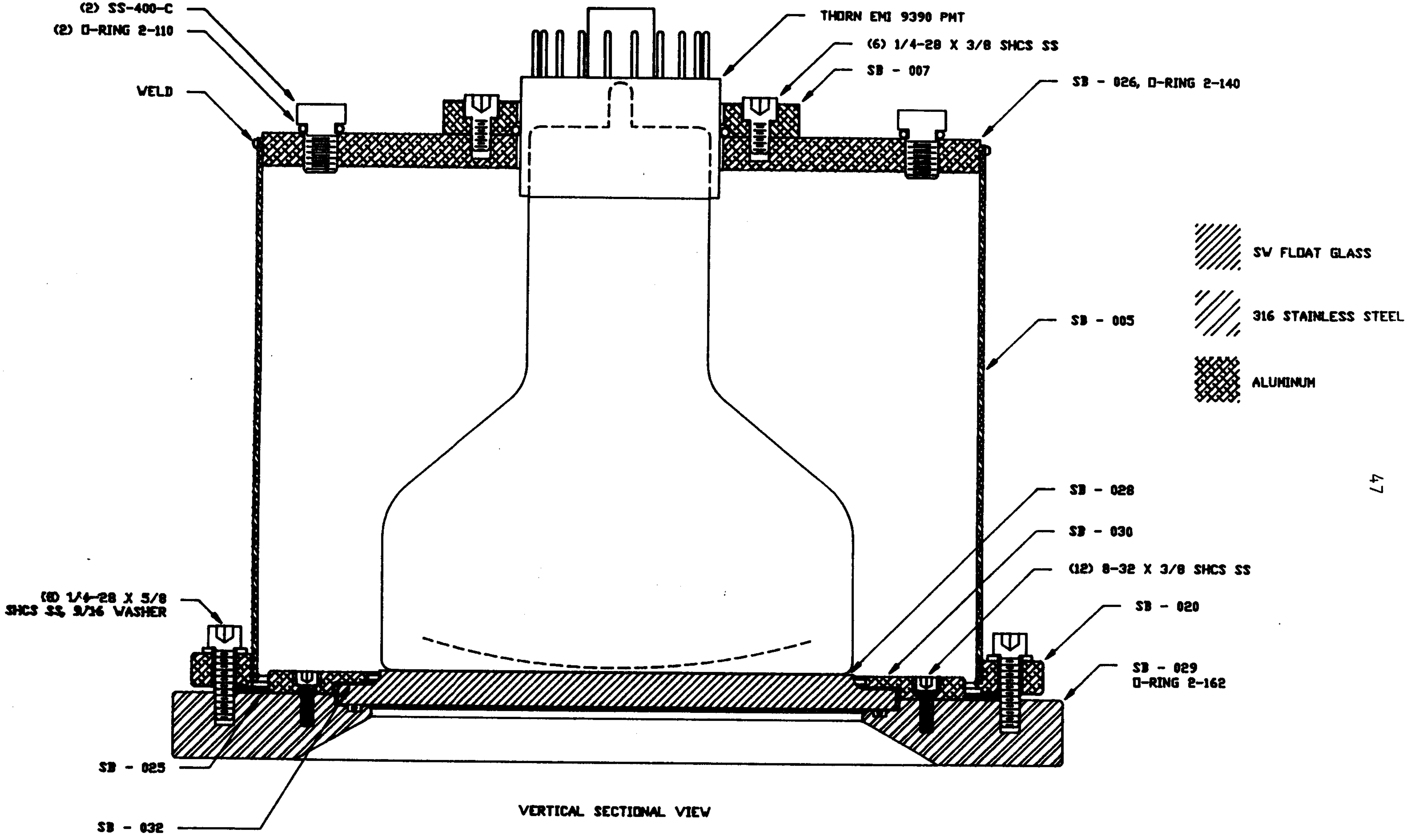
(2) SS-400-C
(2) O-RING 2-110
WELD
THORN EMI 9390 PMT
(6) 1/4-28 X 3/8 SHCS SS
SB - 007
SB - 026, O-RING 2-140
SW FLOAT GLASS
316 STAINLESS STEEL
ALUMINUM
SB - 005
SB - 028
SB - 030
(12) 8-32 X 3/8 SHCS SS
SB - 020
SB - 029
O-RING 2-162
(8) 1/4-28 X 5/8
SHCS SS, 9/16 WASHER
SB - 025
SB - 032
VERTICAL SECTIONAL VIEW

Fig. IV.7: Vertical cross section of a photomultiplier assembly with window flange and housing.

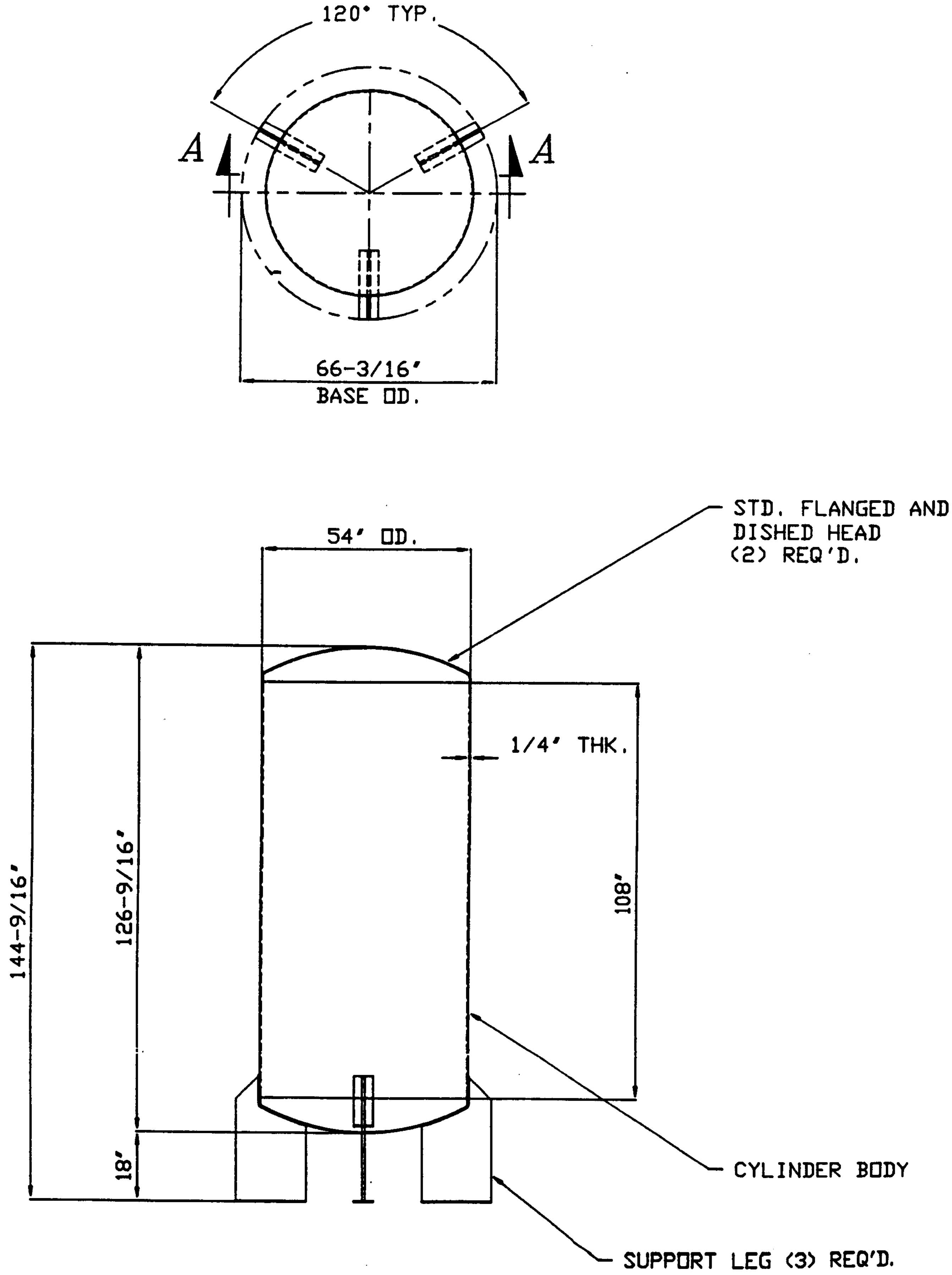
120° TYP.
A
A
66-3/16'
BASE OD.
54' OD.
STD. FLANGED AND
DISHED HEAD
(2) REQ'D.
1/4' THK.
144-9/16'
126-9/16'
108'
18'
CYLINDER BODY
SUPPORT LEG (3) REQ'D.

Fig. IV.8: Horizontal (top) and vertical (bottom) cross sectional view of maintanance tank.

scintillator contents of any of the *SuperBall* tanks. Other auxiliary equipment include 5 stainless steel expansion vessels, one for each tank segment, to allow for an expansion of the scintillator volume, should the ambient temperature rise above the normal level. As a further precautionary measure, each expansion vessel is equipped with a over-pressure safety valve.

V. Liquid-Scintillator and Reflectance Tests

In order to choose an effective liquid scintillator for the *SuperBall* neutron calorimeter, several samples of Gd-loaded organic liquid scintillator, manufactured commercially either by *Bicron Corporation* or *National Diagnostics*, were subjected to various experimental tests. The goals of these tests were to find an economical scintillator with a relatively high light output for a given excitation and, therefore, good energy resolution. The liquid has to be long-term compatible with SS304 stainless steel, the material of the wetted inner tank surfaces, and the emission spectrum had to be matched to the sensitivity of the *Thorn-EMI* 9390KB photomultipliers intended for use with the *SuperBall.* The two scintillators examined more closely are both based on a pseudo-cumene solvent, doped with Gd and several other additives such as wavelength shifters and phosphors. As can be seen from Table 2, the physical parameters of BC-521 and ND-309 are very close to one another. They differ, however, in the nature and concentration of the additives; the exact composition of the scintillator constitutes proprietary information. Yet another, very similar, product, NE 343, offered by *NE Technology, Inc.*, was also considered but, together with the *Bicron* product, was eventually found economically not competitive.

Table 2: Physical Parameters of Tested Gd-Loaded Liquid Scintillators

	Bicron Corporation (BC-521)	*National Diagnostics Inc. (ND-309)*
Solvent Base	1,2,4 Trimethyl-Benzene	1,2,4 Trimethyl Benzene
Gd Content (Weight)	0.2 %	0.2 %
Flash Point	44 °C	49 °C
Density	0.89 g/cm^{-3}	0.89 g/cm^{-3}
Refractive Index	1.50	1.51
Decay Time	3.6 ns	3.8 ns
λ_{max}	424 nm	418 nm
Attenuation Length	> 4 m	> 5 m
Light Output	68 %	62 %
Expansion Coefficient	$4.9 \cdot 10^{-4}$/ °C	$4.9 \cdot 10^{-4}$/ °C

Of the two scintillation liquids, the *BC-521* had been used successfully in the smaller Rochester RedBall neutron multiplicity meter (NMM) for six or seven years, in an application very similar to that intended for the *SuperBall.* Due to the construction and material of the NMM tank, a slow contamination of the scintillator had occurred by iron from the wall of the inner tank surface, escaping through imperfections in the epoxy paint coat of this surface, into the scintillator, leading to a deterioration of its properties. Organic scintillators are extremely sensitive to impurities, especially to oxygen (but not nitrogen) from the air and to metals such as iron and copper(brass). For this reason, stainless steel SS304 was chosen as material for the *SuperBall* tanks, rather than the carbon steel used in the construction of the NMM.